AN ABSTRACT OF THE THESIS OF

Khang Tran for the degree of Master of Science in Mechanical Engineering presented on September 19, 2019.

Title: Development and Application of a Reduced Chemical Kinetics Model for Low-Speed Pre-Ignition Investigation

Abstract approved: _____

Christopher L. Hagen Kyle E. Niemeyer

Gasoline direct injection engines, with downsized boosted technology, present a promising option for enhancing power density and reducing fuel consumption for next-generation engine designs to meet stringent fuel economy and emission standards. However, these developments in the low-speed and high-load operating regime are challenged by the occurrence of a new knocking combustion phenomenon: low-speed pre-ignition. Lubricant oil droplets and their constituents, when diluted with gasoline injection, have been suggested as a key characteristic affecting this phenomenon. We have developed a reduced chemical kinetics model that represents gasoline, lubricant base oil, and oil additive constituents, and validated it against both literature detailed chemical kinetics models and experimental data from jet-stirred reactors and shock tubes. Preliminary application of this reduced chemical kinetics models via direct injection engine simulations at low-speed, high-load operating conditions has triggered pre-ignition event when a lubricant oil droplet is present in the combustion chamber, indicating a promising outlook for this field of research. This study represents the first step in the development of an effective chemical kinetics model able to be incorporated in a multidimensional computational fluid dynamics framework for engine applications and low-speed pre-ignition investigation.

Development and Application of a Reduced Chemical Kinetics Model for Low-Speed Pre-Ignition Investigation

by

Khang Tran

A THESIS

submitted to

Oregon State University

in partial fulfillment of
the requirements for the
degree of

Master of Science

Presented September 19, 2019
Commencement June 2020

Master of Science thesis of Khang Tran presented on September 19, 2019.

APPROVED:

Major Professor, representing Mechanical Engineering

Head of the School of Mechanical, Industrial, and Manufacturing Engineering

---

Dean of the Graduate School

I understand that my thesis will become part of the permanent collection of Oregon State University libraries. My signature below authorizes release of my thesis to any reader upon request.

Khang Tran, Author

ACKNOWLEDGEMENTS

First, I would like to give my sincerest thanks to my advisor, Dr. Chris Hagen, who has been a wonderful scientist/engineer/professor to work for during the course of my Master's degree. Not only did he give me the opportunity to join his research team and produce valuable work, Dr. Hagen's thoughtful guidance, not only for me but all students under his advisement, has helped fostering my academic endeavors tremendously. His constant strive for hard work and scientific excellence continue to inspire me to do my best every day and I'm thankful to have the opportunity to work for him.

I would like to also thank my co-advisor, Dr. Kyle Niemeyer, for his insightful feedback and encouragement during my time here. He has always set a high standard for the research I've done, and his invaluable scientific advisement continues to guide me on my work daily.

Additionally, I would like to thank my lab members: Shane Daly, Zac Taie, and James Benbrook. They have helped me tremendously since my first day here, from finding a place to live, to struggling with me through the courses and projects we did together, as well as helpful discussions about my project even when they're so busy. I'm thankful to have met these people and maintained wonderful friendships with them.

I gratefully acknowledge the Chevron Energy Technology Company for funding this work, as well as the scientists at Chevron for whom I've had the opportunity to work alongside. They have provided wonderful feedback and guidance for the project in which I value greatly.

And finally, I would like to thank my family and friends who have been there every step of the way. You've encouraged me during dark times, and wholeheartedly supported my journey. I wouldn't have been able to accomplish what I've done without your support, and for that I am very grateful. I could go on, but must cut short since this thesis is due any moment now. I hope you continue to watch over me, and I promise to continue making you proud.

TABLE OF CONTENTS

LIST OF FIGURES

Figure Page

LIST OF FIGURES (Continued)

Figure Page

LIST OF TABLES

LIST OF ABBREVIATIONS

CAFE	Corporate Average Fuel Economy
OEMs	Original Equipment Manufacturers
IC	Internal Combustion
GDI	Gasoline Direct Injection
SI	Spark-Ignition
LSPI	Low-Speed Pre-Ignition
SPI	Stochastic Pre-Ignition
EGR	Exhaust Gas Recirculation
BMEP	Brake Mean Effective Pressure
HC	Hydrocarbon
CO	Carbon Monoxide
CFD	Computational Fluid Dynamics
SOC	Start of Combustion
ATDC	After Top Dead Center
PAO	Poly-Alpha-Olefin
ILSAC	Internaltional Lubricant Specification Advisory Committee
API	American Potroleum Institute
EOLCS	Engine Oil Licensing and Certification System
VOF	Volume of FLuid
BDC	Bottom Dead Center
TDC	Top Dead Center
RMG	Reaction Mechanism Generator

PIONA	Paraffins, Isoparaffins, Olefins, Naphthenes,Aromatics
PRFs	Primary Reference Fuels
RON	Reseach Octane Number
MON	Motor Octane Number

Chapter 1: Literature Review

1.1 Introduction

Stringent emission regulations to support energy and environmental issues in recent years, such as the Corporate Average Fuel Economy (CAFE), have pushed automotive industry to develop advanced technology to meet these standards [1]. As a result, in recent years original equipment manufacturers (OEMs) have shifted toward downsizing internal combustion (IC) engines with turbocharging and direct-injected fuel system, namely gasoline direct injection (GDI) engines. These technologies, while utilizing reduced engine displacement volume, offer an effective approach to improving fuel efficiency while maintain adequate performance level by shifting engine operating points into regions of operating map with higher efficiency and subsequently lower specific fuel consumption [2]. Comparing to naturally aspirated engines of similar performance, GDI engines, through the ensuing reductions in friction, pumping losses, and vehicle weight, could reduce the fuel consumption by 12 - 16% [3].

GDI engines take advantage of turbocharging to compensate for a reduced maximum power due to downsizing; operating at these boosted conditions lead to higher specific loading compared to typical spark-ignition engines. This has given rise to a new form of combustion anomaly: low-speed pre-ignition (LSPI) [4], otherwise known as stochastic pre-ignition (SPI) [5], unwanted pre-ignition [6], super-knock [7], developing detonation [8], or subsequent front propagation [9]. Characterized by high-frequency pressure oscillations that follows after a pre-ignition event, as can be seen in Figure 1.1, a single super-knock event can cause severe damages to exhaust valve, piston ring, and spark of an engine. Figure 1.2 shows examples of catastrophic damages caused by super-knock events.

Furthermore, in comparison with conventional knock in SI engines, which arises from auto-ignition of the end gas ahead of spark-triggered propagating flame, super-knock events appear randomly with little direct relationship to engine control parameters such as equivalence ratio, ignition timing, intake temperature, etc [11]. Practical solutions,

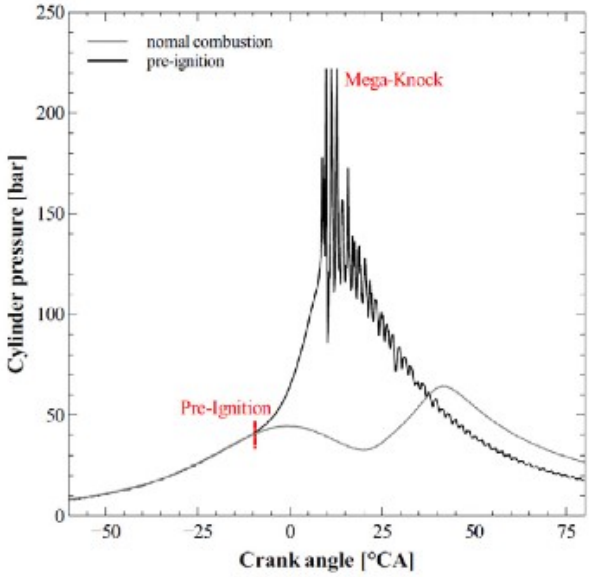

Figure 1.1: Pressure traces of a super-knock event comparing to normal combustion [10].

namely cooled exhaust gas recirculation (EGR) and mixture enrichment, have been applied in the production of gasoline engines as an effort to control super-knock. Amann et al. studied the effect of EGR on super-knock in GDI engines, which showed reduction of super-knock frequency and intensity with 6% cooled EGR, while also increasing brake mean effective pressure (BMEP) when comparing to a baseline case without EGR [4]. Mixture enrichment was also attempted to control super-knock frequency [12, 13]. By injecting excess fuel, the effect of charge cooling is enhanced, and reduction in temperature of the mixture is observed. However, when engines are performed under the condition of fuel enrichment, hydrocarbon (HC) and carbon monoxide (CO) emissions increase, and fuel economy is reduced, offsetting the benefits achieved by using GDI engine technology. Thus, despite ongoing research and development efforts, the occurrence of super-knock events presents a major obstacle for the automotive industry to overcome to further the development of GDI engine technology.

Several theories have been proposed in the literature, attempting to explain the mechanism of super-knock. One theory centers on lubricant oil droplets entering the combustion chamber from the piston top land crevice, leading to super-knock [15]. In this proposed

Figure 1.2: Damaged engine components due to super-knock: a) spark electrode breakup, b) exhaust valve melt, and c) piston ring land broken [14].

mechanism, the lubricant oil is diluted by fuel injection, which increases volatility and promotes droplet vaporization, leading to auto-ignition. Another theory focuses on solid particles/engine deposits, as these products of incomplete combustion could survive engine cycles in the combustion chamber and participate in surface oxidation reactions to become a potential inducement of super-knock [16]. Additionally, other theories (i.e. hot surfaces, trapped end gas from previous engine cycle) have also been reported as triggering sources leading to super-knock events [15].

Among these proposed LSPI mechanism, the effect of lubricant oil droplets, diluted with gasoline direct injection, has received a great deal of attention in the literature [17–21]. Because of the complex formulation of lubricant oil, certain components with faster ignition delay times can increase local reactivity of oil droplets when they enter the combustion chamber. Under appropriate temperature and pressure conditions, and in combination with dilution from fuel direct injection, the oil droplets can self ignite, leading to pre-ignition and potentially a super-knock event.

While a plethora of experimental evidence has been found to support these mechanisms, minimum computational modelling work is present in the literature to provide a parallel effort in super-knock mitigation and GDI engine development. Multi-dimensional Computational Fluid Dynamics (CFD) tools present a cost-effective way to study a wide range of parametric space, physical and chemical processes, as well as detailed in-cylinder information, which is normally not available or accessible in an experimental engine setup [22]. However, accurately modeling the combustion of the fuel mixture requires a detailed chemical kinetic model, which can consist of thousands of species and tens of thousands

of elementary reactions to describe complex liquid transportation fuels. Models of such large sizes would induce prohibitive computational costs in high-fidelity multidimensional engine simulations.

This work aims to develop and use a reduced chemical kinetics model, one that includes representation of gasoline, lubricant base oil, and oil additives in a three-dimensional CFD framework to investigate the effect of lubricant oil droplets on LSPI. In doing so, current super-knock suppression strategies such as mixture enrichment can be minimized, leading to higher fuel efficiency and lower emission, complimenting the benefits that come with utilizing GDI engine technology.

1.2 Pre-ignition, conventional knock, and super-knock

In the current body of research involving knocking combustion, the terms "pre-ignition" and "super-knock" have both been used interchangeably to describe engine knock occurring in low-speed, high-load conditions in GDI engines. However, they represent two different combustion phenomena and distinction between the two is necessary. "Pre-ignition" represents the combustion of air/fuel mixture triggered by hot spots in the combustion chamber, other than the electric spark coming from the spark plug [23]. Pre-ignition causes the cylinder pressure to increase above the compression pressure prior to spark plug firing, leading to rapid rising of pressure and temperature of the unburned gas. If auto-ignition occurs in this high-pressure, high-temperature mixture, an extreme knock event can occur, and is often referred to as "super-knock" in the literature. Nevertheless, in addition to super-knock, pre-ignition may cause different combustion phenomena, including non-knocking combustion phenomena, depending on pre-ignition conditions.

Wang et al. conducted an experimental investigation on a turbocharged gasoline direct injection engine in order to differentiate between pre-ignition and super-knock [14]. Using Δp, defined as the peak pressure value obtained by high-pass filtering of the original pressure curve, the authors quantitatively classified engine knock into three different categories: super-knock where $\Delta p > 2$ MPa, heavy-knock in which 0.2 MPa $< \Delta p < 2$ MPa, and slight-knock where $\Delta p < 0.2$ MPa. Figure 1.3 shows the variation of start of combustion for different engine cycles studies by Wang and his colleagues, where the start of combustion (SOC) is defined as the corresponding crank angle of the 10% fuel mass burned fraction. Additionally, the cycles with SOC earlier than 18 degrees crank

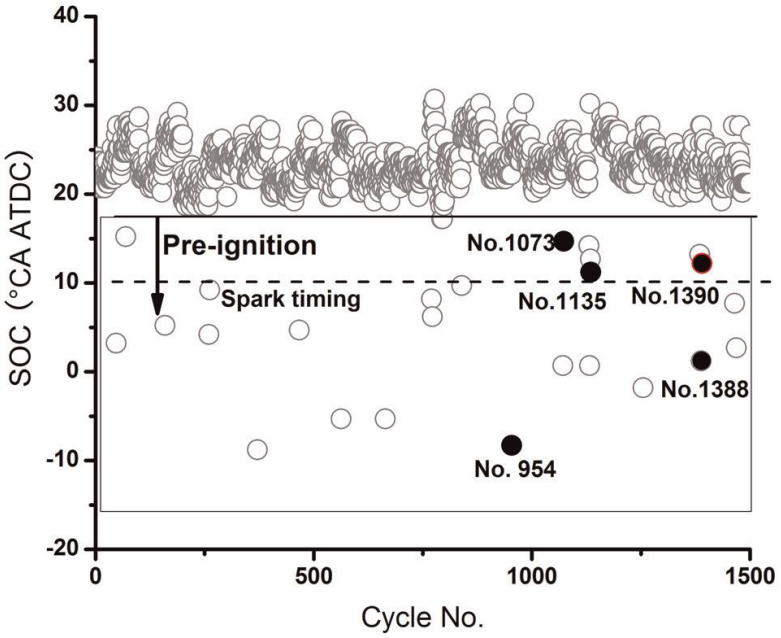

Figure 1.3: Variation of start of combustion [14].

agles after top dead center (ATDC) are considered as pre-ignition cycles, highlighted inside the rectangular section in Figure 1.3. Combining this pre-ignition window with the qualitative classification stated above, Wang et al. observed that pre-ignition, while always happens for a super-knock cycle (cycles 954 and 1388), could also lead to heavy-knock (cycle 1135), slight-knock (cycle 1390), or non-knock (cycle 1073).

"Super-knock", severe engine knock triggered by stochastic pre-ignition, is named to distinguish from "conventional knock", a combustion phenomenon due to end-gas auto-ignition prior to spark-triggered flame propagation in the combustion chamber [24]. Figure 1.4 shows the pressure trace comparison between super-knock, conventional knock, and normal combustion. By looking at the amplitude of peak pressure rise, a distinction can be made between conventional knock and super-knock, where the maximum pressure rise value of super-knock ($\Delta p = 12$ MPa) can be an order of magnitude higher than that of conventional knock ($\Delta p = 0.5$ MPa). Additionally, in comparison with normal combustion, the peak pressure of super-knock can exceed three times higher, leading to catastrophic engine damages.

Subsequently, using the magnitude of pressure oscillation, Wang et al. categorized SI

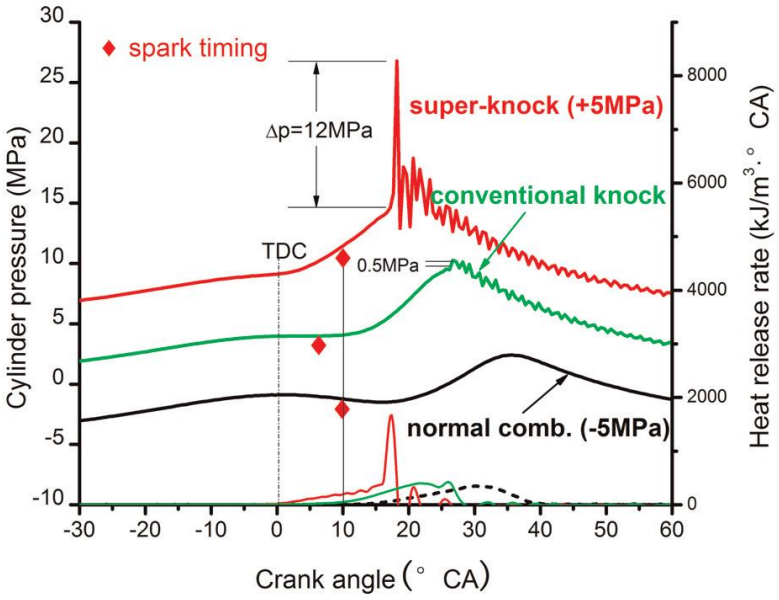

Figure 1.4: Pressure traces comparison between super-knock, conventional knock, and normal combustion [14].

combustion into normal combustion (non-knock) and engine knock. Furthermore, engine knock can be classified into two categories: super-knock and conventional knock. Depending on the mode of auto-ignition, super-knock can be broken down even further.
In conclusion, pre-ignition and super-knock, while used interchangeably to describe engine knock caused by stochastic pre-ignition, are two different combustion phenomena. While pre-ignition events are the origin of end-gas detonation, they do not always lead to a super-knock event, but can also bring about end-gas deflagration (heavy-knock, slight-knock) as well as non-knock phenomenon (normal flame propagation and combustion). Therefore, a pre-ignition event does not always lead to super-knock in GDI engines, but a super-knock event is always originated from a pre-ignition event.

1.3 Possible pre-ignition sources leading to pre-ignition and super-knock

Within the literature, several bodies of research have been conducted to identify the causes of super-knock [15, 25–27]. Three possible sources have been proposed as the inducements of pre-ignition events: surface ignition, solid particles/engine deposits, and lubricant oil droplets. Detailed discussions are now provided in the following paragraphs.

1.3.1 Surface ignition

High temperature locations within the combustion chamber (i.e. exhaust valves, spark plug, etc.), or "hot spots", have been proposed in the work of Dahnz et al. to be a potential source for pre-ignition [15]. When a hot spot is present in the combustion chamber, it can increase the local temperature and induce a pre-ignition event. In their work, Dahnz and his colleagues performed optical investigations to evaluate whether spatial distribution of pre-ignition origins could be structured due to hot spots.

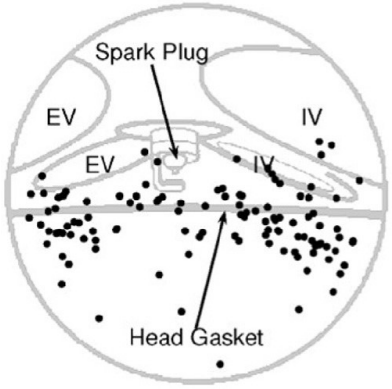

Figure 1.5: Spatial distribution of pre-ignition origins [15].

By looking at endoscopic data plotted on top of visible combustion chamber outlines, as can be seen in Figure 1.5, where each black dot indicates the starting point of one optically registered auto-ignition, the authors concluded that pre-ignition origins are independent to that of the locations of hot spot in the combustion chamber (i.e. spark plug, valves). By means of detailed analyses, Dahnz et al. showed no significant correlation

between the engine operating conditions and the distributions of pre-ignition origin, as the registered starting points of combustion are spread over a wide range throughout the whole combustion chamber.

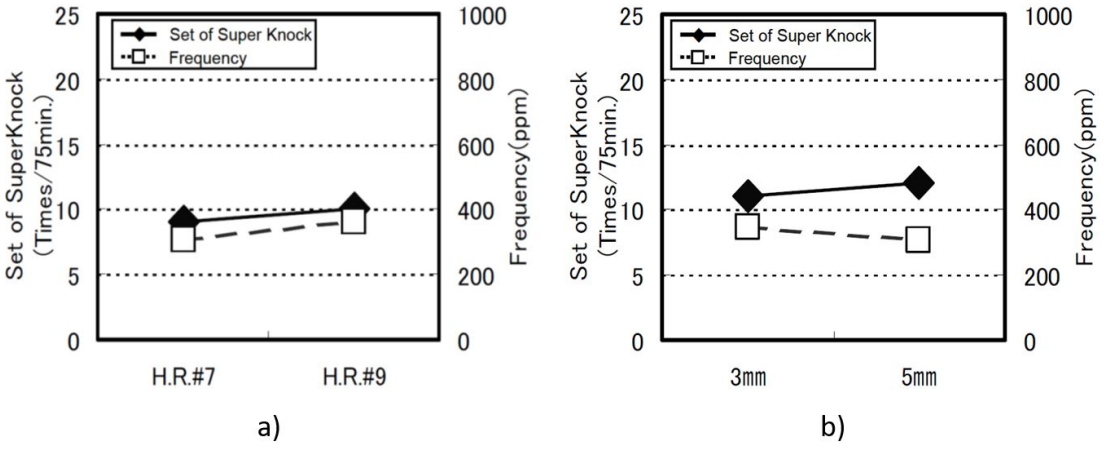

Figure 1.6: Influence of different spark plug features on super knock: a) Heat range and b) Ignition point [28].

Additionally, Inoue et al. conducted experimental studies using an in-line four-cylinder SI engine with direct-injection and turbo-charging to investigate the influence of spark plug characteristics on super-knock [28]. With its high temperature from exposure to combustion gas in the chamber, it is possible for spark plugs to induce pre-ignition events that could potentially lead to super-knock. The experiments were conducted under conditions of low speed and high load where super-knock is likely to occur. Furthermore, the author disconnected the blow-by hose to eliminate the effect of engine oil droplets entering the combustion chamber.

Figure 1.6 shows the influence of different spark plug features on the frequency of super-knock. Here, the authors looked at the influence of spark plug heat range, comparing type 7 (suitable for test engine with a measured center electrode temperature of 532°C) with type 9 (colder typle with measured center electrode temperature of 440°C) and found no significant difference in super-knock frequency despite the temperature difference of about 100°C. Different spark plug ignition points were also under investigation in their work. Inoue et al. studied spark plugs of heat range 7 with ignition projection points of 3mm

and 5mm, and arrived at similar conclusion as their previous study on spark plug heat range. Additional features, such as ground electrode length, center electrode diameter, extended metal shell, and presence of electrode copper core were also investigated. From these results, Inoue et al. concluded that despite variation in different spark plug features, no significant difference in super-knock frequency was found, leading to their conclusion that spark plug has no significant influence on super-knock.

1.3.2 Solid particles/Engine deposits

The presence of solid particles in the combustion chamber has a close connection with pre-ignition. As a product of incomplete combustion, solid particles can survive an engine cycle, stay in the combustion chamber, participate in surface oxidation reactions in the next cycle, and become a local hot spot for mixture ignition. Okada et al. first proposed a super-knock mechanism from examining results of in-cylinder visualization when injecting deposit flakes of varying diameters, including those obtained from the combustion chamber, combustible and non-combustible substances (i.e. $CaSO_4$, cigarette ash, carbon black) [16]. Figure 1.7 details the description of this mechanism.
In this proposed mechanism, deposits formed by cylinder liner wall wetting (A) and deposits formed at low engine operation loads (B) peel off and float into the combustion chamber (C). At this point, these deposits go through engine cycle, get exposed to combustion, burn in flame propagation (D) and extinguish between the expansion and exhaust strokes (E). If these deposits survive and remain in the combustion chamber, surface oxidation reactions will continue to occur. With introduction of new oxygen from the intake stroke as well as acceleration of oxidation reactions from the compression stroke, glowing particles are now present in the combustion chamber (F). Finally, when the energy required for ignition of the surrounding mixture is discharged, combustion of said mixture occurs (G).
Similar findings have also been found in the literature to support this super-knock mechanism. Kuboyama et al. utilized direct-photography of pre-ignition events by means of an endoscope to investigate the mechanism of super-knock induced by solid particles [21]. In this body of research, the authors reported observation of glowing particles during the early stage of compression stroke, in which they induced pre-ignition before spark ignition timing; these results can be seen in Figure 1.8. Lauer et al. also performed

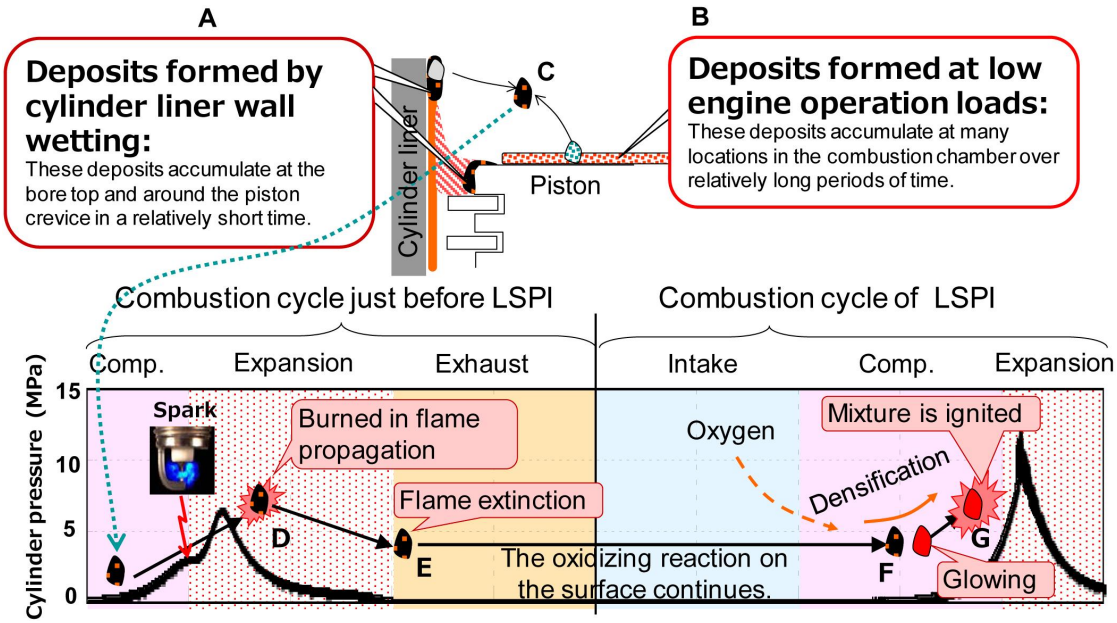

Figure 1.7: Super-knock-induced mechanism from solid particles [16].

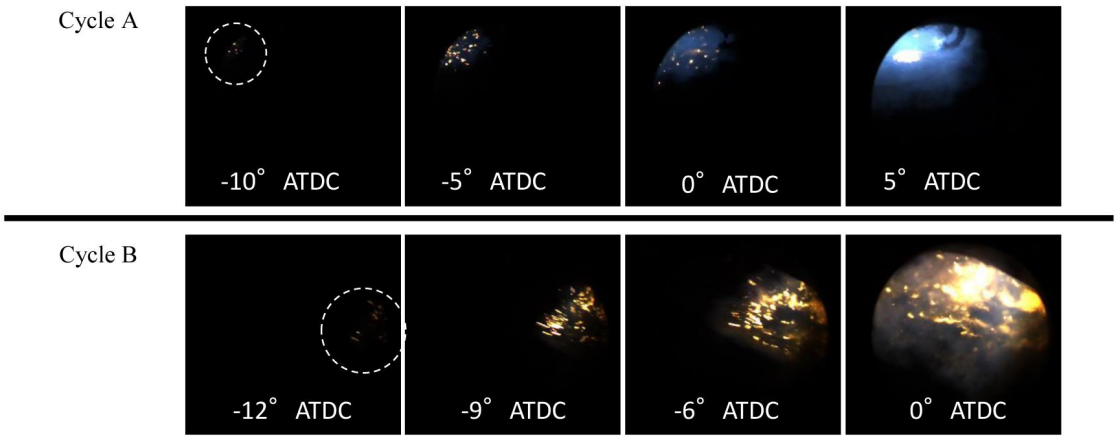

Figure 1.8: Direct photographs of pre-ignition from piston crevice area [21].

optical diagnostics on a turbocharge 4-cylinder, direct-injection test engine, and observed glowing particle surviving engine cycles to provoke pre-ignition events in the next cycle [29].

1.3.3 Lubricant oil droplets

Modern lubricants, formulated from a range of base fluids and chemical additives, provide the necessary fluid layer in between moving engine surfaces to keep friction at a minimum as well as remove heat and wear particles [30]. However, certain components within the lubricant oil, having shorter ignition delay time, can increase local chemical reactivity of oil droplets when they enter the combustion chamber. Under appropriate temperature and pressure conditions, and in combination with dilution from fuel direct injection, the oil droplets can self-ignite, lead to pre-ignition and potentially a super-knock event. Dahnz et al. first proposed a droplet ignition theory, centering around the influence of droplets with high-boiling, highly ignitable components potentially coming from the lubricant oil [15]. Due to their evaporation, regions surrounding these droplets can have reduced ignition delay times compared to the ambient gas. This hypothesis was further supported by the work of Kalghatgi et al., claiming long-chain molecules of the oils to be associated with shorter auto-ignition delay times [31]. Figure 1.9 presents a hypothesis for mechanism of oil detachment from the piston crevice volume, proposed in the work of Mayer et al [10].

In this proposed detachment mechanism, the impact of fuel direct injection and wall wetting are highlighted in Step 1. In addition to lubricant oil dilution, fuel direct injection also contributes to reduced viscosity at the wall, as well as surface tension and flashpoint. Once enough accumulation is present in the piston crevice volume, as shown in Step 2, depending on the boundary conditions at the cylinder walls, three oil detachment possibilities are presented in Step 3 of this mechanism. Oil droplets can be introduced to the combustion chamber by means of reverse blow-by at exhaust valve opening, splashing caused by impinging fuel spray, or due to piston movement near top dead center. Mayer et al. argued that dilution and accumulation by means of fuel injection are essential for the subsequent detachment of droplets because of the effects of dilution, wall wetting, and subsequent reduced viscosity effects on lubricant oil droplets [10]. Additional studies carried out by Zahdeh et al. and Amann et al. further confirmed this hypothesis by

looking at fuel injection stratery, spray target, as well as piston geometry effects on fuel and oil accumulation in the crevice volume [23, 32]

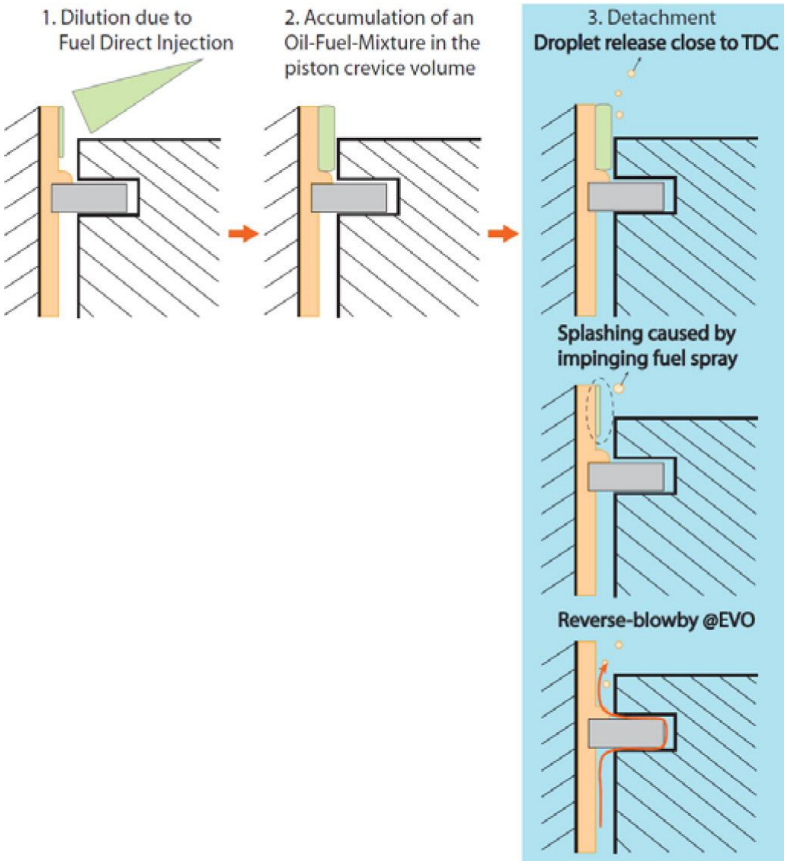

Figure 1.9: Detachment of oil droplet from piston crevice [10].

Once the oil droplets are released from the piston crevice area and enter the combustion chamber, a combustible mixture can be formed around the droplet via vaporization, leading to a pre-ignition event when the temperature for mixture auto-ignition is reached. This process, detailed in the work of Takeuchi et al., is illustrated in Figure 1.10 [17]. Extensive experimental research have been carried out in the literature as an effort to verify this hypothesis. Hirano et al. used a turbocharged DI-SI to evaluate the effect of different lubricant base oils, as well as different engine oil additives on super-knock [33]. Their results showed an increase in LSPI frequency when a Poly-Alpha-Olefin (PAO)

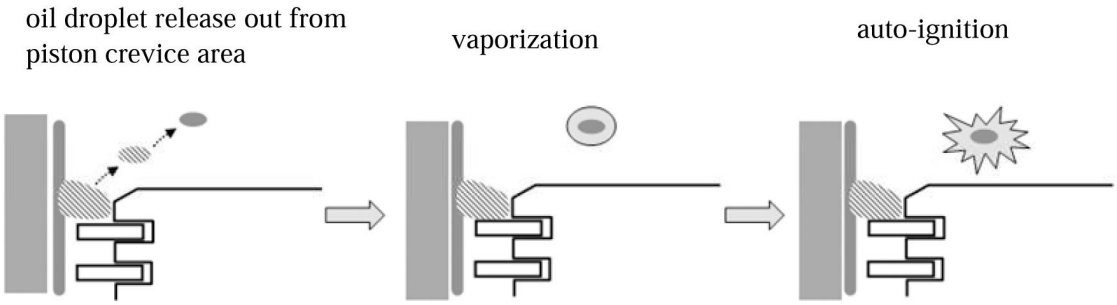

Figure 1.10: Mechanism for lubricant oil droplets inducing LSPI [17].

base oil of higher viscosity was used. Furthermore, comparison between two different groups of lubricant oil confirmed the effect of metal-based detergent additive, showing higher super-knock frequency when an oil with a detergent package is used in a GDI test engine.

Additionally, lubricant oil additives, specifically metal-based additives, have been reported to correlate directly with the frequency of super-knock due to possible catalytic reactions. While metallic detergent additives such as Ca-sulfonate significantly increase the frequency of super-knock event, other additives which work as anti-oxidants (i.e. ZnDTP, MoDTC) were confirmed to show a performance benefit to reduce super-knock when added to the formulation of lubricant oil. Study conducted by Fujimoto et al. showed a significant increase in super-knock frequency when a higher mass percentage of Ca-detergent was used [34]. Conversely, the higher usage of ZnDTP or MoDTC provided a preventative effect on super-knock events. These results were again seen in a different study, conducted by Ritchie and his co-workers [35]. Figure 1.11 details the findings of these studies.

Different metal-based additives were also investigated in the assessment of their effect to the frequency of super-knock events in GDI engines. It was found that the addition of Fe and Cu compounds, as well as additive packages containing Na, showed contributory effects on super-knock frequency, whereas the addition of K-containing or Li-containing compounds to the formulation of lubricant oil helped reducing the frequency of super-knock events [17, 33, 34, 36, 37]. Therefore, optimizing lubricant oil formulations in an effort to suppress super-knock, while keeping the inherent benefits (i.e. anti-wear and anti-oxidant properties, corrosion inhibition, friction reduction) of an effective lubricant oil blend presents a promising area of research.

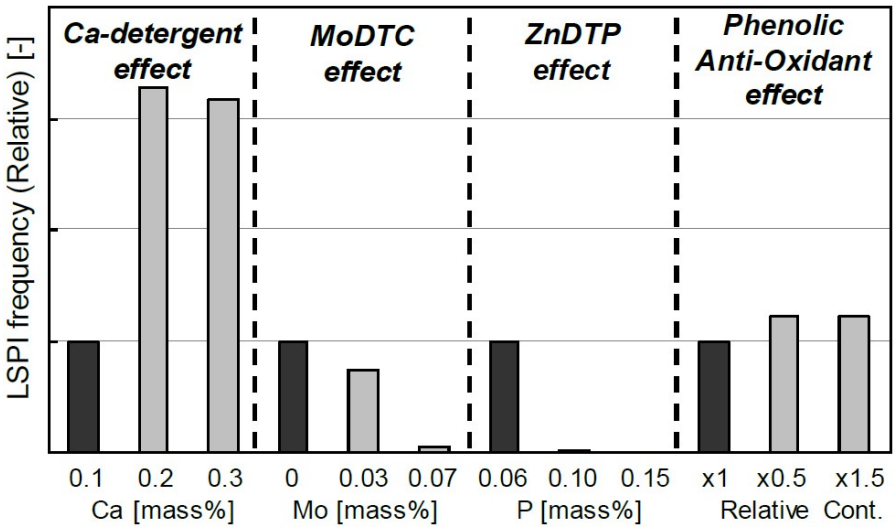

Figure 1.11: Effects of engine oil additives on super-knock frequency [34]

Performance specification used to quantify the quality of gasoline engine oils for North American and Japanese auto companies is determined by the International Lubricant Specification Advisory Committee (ILSAC), as well as the American Petroleum Institute Engine Oil Licensing and Certification System (API EOLCS) [38]. In preparation for modern engine development that comes with downsizing and turbocharging (i.e. GDI engines) as well as the technical challenges that arise from such technology (i.e. pre-ignition and super-knock), a new engine oil regulation, the ILSAC GF-6, is currently underway for adaptation in the development of future lubricant oils. Replacing the current ILSAC GF-5 specification, the proposed GF-6 standard contains series of new tests that would ensure enhanced performance level of lubricant oil for SI engines, specifically in terms of fuel economy, wear and tear, enhanced oil robustness, and most importantly, protection against the occurrence of super-knock [39].

Figure 1.12 presents the Ford Motor Co. 2012 Explorer 2.0L turbocharged GDI engine used for LSPI investigation in the ILSAC GF-6 standard. This test engine features variable camshaft timing, dual overhead camshafts driven by a timing chain, four valves per cylinder, as well as electronic direct-fuel injection. Described as a “flush and run” test, the test engine is used for multiple tests, and the next test oil is used to flush the previous test oil from the engine. The test procedure is conducted in four iterations,

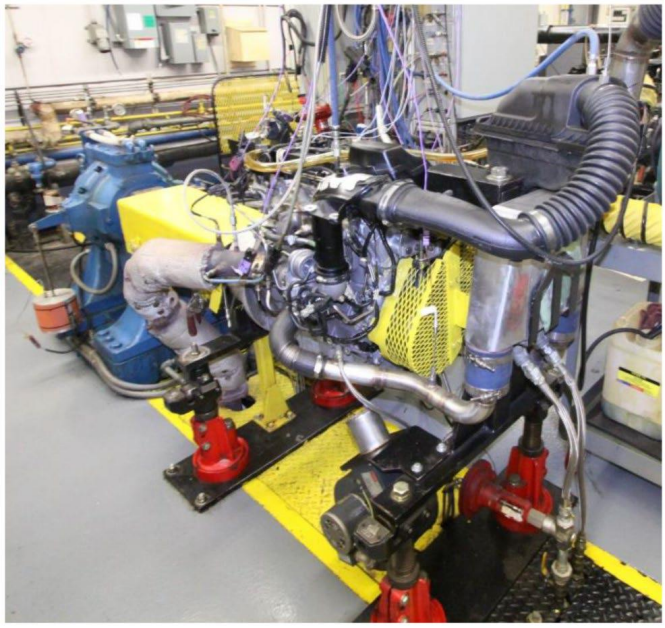

Figure 1.12: Sequence IX test stand with engine [39].

with 175,000 engine cycles in length per iteration. Pre-ignition events are then generated through low-engine speed, high-load, and steady-state conditions. These events are then counted throughout each of the four 175,000 engine cycles. Finally, combustion pressure is measured directly in each cylinder of the test engine to provide documentary evidence of the occurrence of pre-ignition events.

These upcoming standards, while providing a new performance level (i.e. super-knock resistance) for future engine oil formulation in internal combustion engines, require time consuming and expensive physical experiments in the process. A 2012 Ford 2.0 L Ecoboost engine is needed for testing, and additional modification has to be carried out to ensure data collection is optimum. Furthermore, constant maintenance is required for these test engines, and each test demands exhaustive time-consuming effort. This opens up new venue for the development of a cost-effective and efficient modelling tool, namely a multi-dimensional CFD model, capable of investigating the impact of engine oil and its lubricant additives to super-knock.

1.4 Current Effort in Super-Knock Modeling

In light of the discussion provided in section 1.3.3, having accurate and cost-effective engine simulations as supplement to experimental engine testing could expedite super-knock investigation and development of GDI engines. Currently in the literature, several studies have been reported, using numerical simulation framework, to simulate pre-ignition and/or super-knock events. Peters et al. performed numerical CFD simulations of the gas exchange process in a spray-guided spark-ignition direct-injection gasoline engine using the three-dimensional GMTEC-ACFLUX code based on a standard k-ϵ turbulence model [40]. Following the theoretical framework proposed by Kalghatgi and Bradley, the authors investigated three different cases, one standard case and two super-charged cases using PRF85 as surrogate for gasoline [41]. Coupled with a refined theory of turbulence, namely the dissipation element analysis, Peters et al. were able to predict the joint probability density of the temperature gradient, as well as calculate the detonation probability at each grid point in the CFD simulation in order to determine a maximum detonation probability in the combustion chamber.

Researchers from Chiba University also performed numerical simulation in an attempt to understand the reasons of how a pre-ignition event occurs in a highly boosted gasoline engine [42]. The authors theorized that $CaCO_3$, an oil additive of high interest in the research of super-knock, when added in the formulation of lubricant oil as an additive, may be converted to CaO by heating during the expansion and exhaust strokes. Thereafter, CaO will be converted into $CaCO_3$ again by absorbing CO_2 during the intake and compression strokes. An exothermic reaction, this chemical change can lead to increase in temperature of $CaCO_3$ particle in the upward of 1000K and potentially lead to a pre-ignition/super-knock event when acting as a hotspot in the combustion chamber. Using ANSYS Fluent with a reduced PRF chemical mechanism from Tsurushima et al., the authors implemented the volume of fluid (VOF) method to model oil droplets [43]. Assuming oil droplets scattering from the thin oil film attached on the piston top-land, the authors incorporated different parameters (i.e. thickness of oil film, mixed ratio of oil and gasoline) and numerically simulated the process of oil film moving onto piston top-surface as well as oil droplets coming out into the cylinder.

From this study, researchers at Chiba University confirmed existing hypothesis in the literature regarding the effect of oil droplets on super-knock. Their numerical simulations

showed that droplet particles with a high temperature profile can be a pre-ignition source under real engine condition. However, because of the lack of a chemical kinetics model for $CaCO_3$, no chemical mechanism involving the oxidation and combustion process of said additive was used in this study; instead the chemistry of n-heptane was implemented to model oil droplet within the simulation.

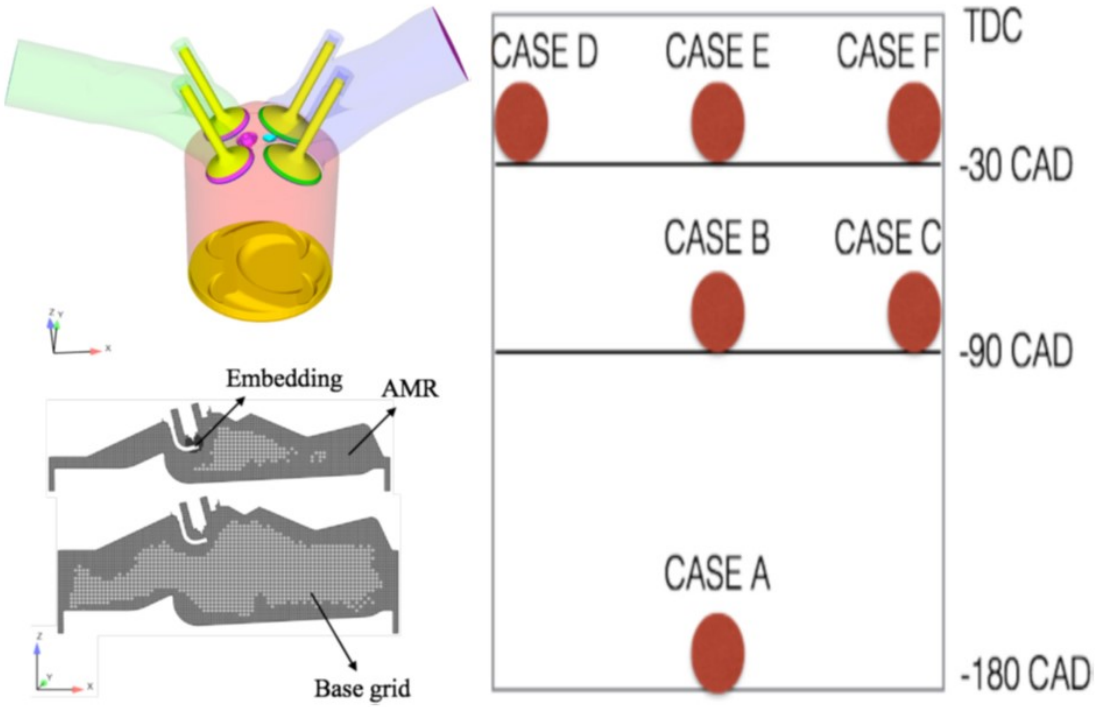

Figure 1.13: AVL SI engine, grid generation, and representation of the location and timing of the hotspot at various positions inside the cylinder [44].

Most recently, Ali et al. performed full-cycle engine simulations using the commercial CONVERGE CFD software, and were able to successfully reproduce the occurrence of super-knock depending on the timing of the pre-ignition events [44]. Within this study, the authors investigated the effect of location and timing of hotspot inside the combustion chamber. Defined as a spherical patch region of radius 1mm with Gaussian temperature profile of 2000 K, the hotspot was introduced at the edge of piston momentarily and removed from the domain due to movement of piston towards the top dead center (TDC).

These locations, timings, as well as the engine geometry and mesh used in this study can be found in Figure 1.13. The authors determined that at late hot spot timing, a pre-ignition event could lead to super-knock. Furthermore, in their case study of the effect of hot spot location, the geometry of the combustion chamber was found to also be important in ascertaining super-knock cycle during a pre-ignition event.
Additional studies were carried out by Ali et al., attempting to investigate the characteristics of pre-ignition cycle with different intake pressures [45]. Set of parametric simulations was conducted with boosted intake pressure of 2 bar in addition to normal pressure at 1 bar, leading to an increase in the maximum peak pressure at late pre-ignition timings. When 25-40% of the fuel is consumed for 1 bar and 2 bar intake pressures, respectively, the flame propagation speed rapidly accelerated regardless pre-ignition cases. The authors attributed this to the increase in the end gas temperature, leading to transition of deflagration front to spontaneous auto-ignition front. However, no chemical kinetics model was used in their work to represent droplet of oils entering the chamber, including representation of lubricant oil additives. Therefore, development of a chemical kinetics model that contains representation of lubricant oil and its additive constituents, currently not available in the literature for modeling effort, is necessary to further this field of LSPI research.

1.5 Intent of Work

The goal of this work is to develop a reduced chemical kinetics model containing representation of gasoline, lubricant base oil, and an oil additive package of interest to super-knock research. In doing so, a multi-dimensional CFD study, incorporating this developed chemical kinetics model, can be carried out to further understand the underlying physics of super-knock and provide parallel effort to experimental investigation in the development of next-generation IC engine technology.

Chapter 2: Reaction Mechanism for Super-Knock

In the following sections, first an introduction of the current efforts conducted in the literature towards a chemical mechanism for super-knock simulation is covered. Secondly, the development and validation of OSU super-knock reaction mechanism is presented.

2.1 Super-Knock Reaction Mechanism Development in the Literature

A chemical kinetic model that can capture the influence of gasoline, lubricant oil, and its constituents on LSPI is necessary for modeling and predicting the onset of super-knock events. The literature currently lacks much research towards measuring ignition delay times of lubricant oils, and more importantly, an effective kinetic model dedicated towards modeling LSPI. However, some groups have studied the effects of additives. Zhang et al. [46] developed a kinetic model to study the antiknock tendency of substituted phenols as additives via an application of the automated reaction mechanism generator (RMG) software. Using a flux-based model enlargement algorithm, the software inputted the interested core species at specified conditions to propose possible reactions and products in the model edge. They chose *n*-butane as the base fuel and generated the model for 1 bar and 650–2000 K. They also generated six models for the blends of substituted phenols for the additive/butane blends, each with 2% mole fraction of the additive under the conditions of 20 bar and 650–2000 K with an equivalence ratio of one. Table 2.1 details the size of the sub-models, as well as the final mergerd model from their work.
Zhang et al. simulated ignition delay studies in a constant volume batch reactor, and their results indicated some of the additives have opposite performance in different temperature ranges. Additionally, they performed sensitivity analysis (i.e. reaction pathway analysis) and determined the anti-knock ability of phenols mainly originates from their ability to quench OH radicals or precursors effectively as the additives are converted into a conjugated ketone. The authors then used the differences in the formation of conjugated ketone and subsequent secondary chemistry to explain the anti-knock ranking of the additives considered in their study. This kinetic model shows good consistency between

Table 2.1: Size of sub-models and merged model from the work of Zhang et al. [46].

Fuel additive	Number of species	Number of reactions
p-Cresol	353	10220
m-Cresol	490	10092
o-Cresol	328	6690
2,4-Xylenol	406	7461
2-Ethylphenol	459	10080
Guaiacol	549	11607
Merged model	1465	27428

predictions and experimental results, useful for ranking the studied anti-knock additives, but is not realistically usable in three-dimensional CFD simulations due to its large size: 1465 species and 27428 reactions. Furthermore, the additive package described in this model is not among those of interest in the research of super-knock.

Most recently, Distaso et al. [47] published a detailed kinetic model for their investigation of lubricant oil influences on ignition of gasoline-like fuels. Containing 7182 species and 31721 reactions, the model was developed starting from existing models available in the literature. They combined the reduced primary reference fuel (PRF) model of Wang et al., containing 73 species and 296 reactions, with the model for 2-methyl-alkanes up to C_{20} and *n*-alkanes up to C_{16} of Sarathy et al. [48, 49]. Distaso et al. performed thorough analysis of reactions and species involved in the two original mechanisms to ensure that the merging process did not affect the agreement with the experimental data originally used in the validating process of said mechanisms.

Different mixture compositions between iso-octane (iC_8H_{18}), n-hexadecane ($iC_{16}H_{34}$), and n-octadecane ($iC_{18}H_{38}$) were numerically simulated with a zero-dimensional homogeneous constant-volume reactor and compared to experimental data of mixtures of iso-octane with lubricant oil. This confirmed the effectiveness of the developed model in reproducing lubricant oil effects on the ignition propensity of iso-octane. Furthermore, they concluded that a surrogate binary mixture composed of n-hexadecane and n-octadecane, taken in the same proportions, can reproduce with good accuracy the higher reactivity of lubricant-fuel mixtures over pure iso-octane. However, the size of this model is also unrealistically large for engine simulations, in addition to its lack of a lubricant oil additive package (i.e., Ca, Mg, Na, ZnDTP) necessary for investigating the effect of these substances on

super-knock propensity.

2.2 OSU Super-Knock Reaction Mechanism

Recognizing the lack of LSPI chemistry models in the literature, this work sought out to develop a reduced chemical kinetic model, suitable for the investigation of LSPI, by combining different sub-models representing the chemistry of gasoline, lubricant base oil, and oil constituents. The following sections detail the main sub-models included in the model for modeling gasoline, engine oil, and its additive constituents.

2.2.1 Gasoline Surrogate Model

Gasoline chemical composition, comprised of hundreds of hydrocarbon species, is complex. Distilled from crude oil, the initial cut of gasoline contains several different classes, including C_4 to C_{10} n-paraffins, isoparaffins, naphthenes, and aromatics. With multiple refinery processes introduced into the mix, the final gasoline product, containing high-octane quality molecules in the gasoline molecular weight range, provides an upgrade over that of crude distillation products. Figure 2.1 details the typical distribution of PIONA (paraffins, isoparaffins, olefins, naphthenes, aromatics) found in U.S. market gasoline fuels, as well as representative molecular structures of these classes.

In addition to hydrocarbon components, gasoline fuels may also contain various oxygenated additives. Consequently, the complexity of gasoline makes it difficult to study computationally. In the interest of numerical investigations, gasoline is typically represented with a surrogate model, often comprising a small number of compounds to create a mixture that matches the physical and chemical properties of a real fuel.

In this body of work, the skeletal kinetic model for primary reference fuel (PRF) developed by Liu et al. was utilized to represent gasoline. Using a new practical approach, namely the "semi-decoupling" methodology, Liu et al.'s skeletal model keeps the number of species as few as possible while maintaining its good performance in various reactors and under wide operating conditions.

The authors carried out extensive model validation effort, using a zero-dimensional gas-phase kinetics program from CHEMKIN PRO, to match up simulated results with those of experimental nature available in the literature. Various experimental data, including

shock tube, jet-stirred reactor, flow reactor, premixed laminar flame speed, and internal combustion engines over a wide range of temperatures, pressures, and equivalence ratios were used by Liu et al. in the validation process. Figure 2.2 highlights a few key comparison between modelling results and experimental data from Liu et al. for various PRF mixtures.

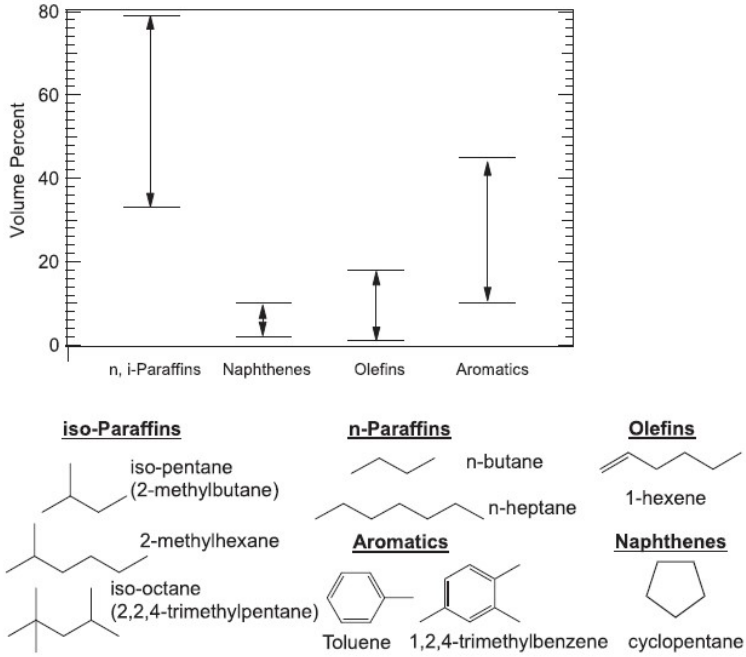

Figure 2.1: Typical PIONA range for U.S. market gasoline fuels, with representative molecular structures in gasoline fuels [50].

The reported results agree well with the experimental data considered, indicating a promising model for various engine applications when integrated in a multi-dimensional CFD model. The final model, consisting of 41 species and 124 reactions, provides a good representation for gasoline in the current work while keeping the model size compact for implementing in three-dimensional CFD. Full details on this kinetics model can be found in Appendix 5 of this work.

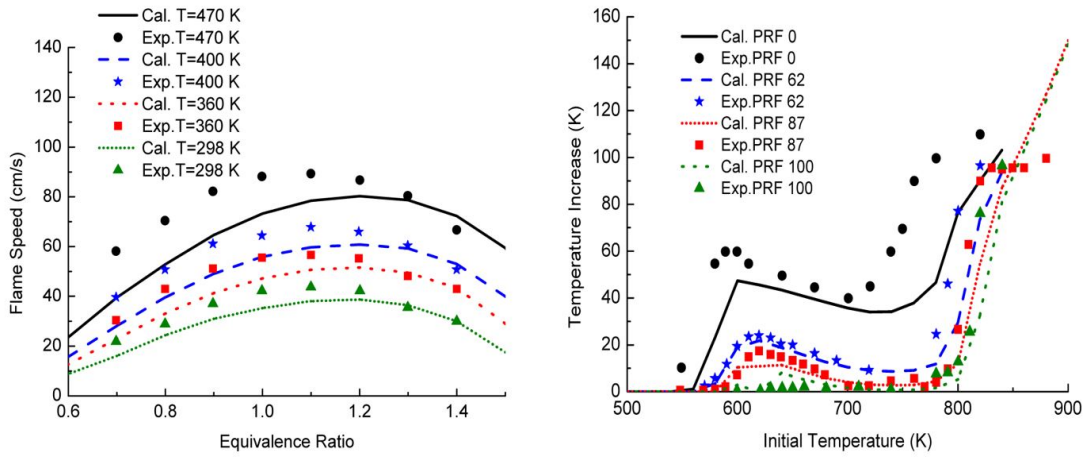

Figure 2.2: Laminar flame speed and flow reactor temperature rise comparison for various PRF blends from Liu et al. [51].

2.2.2 Lubricant Base Oil Surrogate Model

Modern engine oils are comprised mainly of base oils, supplemented with additives intended to improve performance beyond what base oils alone are able to offer [30]. Amann and Alger reported that the main constituents of lubricant oils are about 90%vol and above of lubricant base stock with various additives to reduce friction wear, decrease oxidation tendencies, as well as modify viscosity [25]. Furthermore, lubricant base oils are categorized into five different groups via the API standards. Interested readers are directed to the following publication for additional information on this field of research [52].

Fundamental chemical kinetic modeling studies conducted by Westbrook et al. [53] and Sarathy et al. [49] showed that alkanes larger than C_{14} exhibit nearly identical fuel/air gas-phase ignition delay times across a range of operating temperatures. Conclusively, they proposed that ignition propensity and kinetics of lubricant base oils can be adequately represented by surrogate components comprising linear alkanes of carbon number range of C_{15}–C_{20}. Additionally, Kuti et al. performed a fundamental investigation into the relationship between lubricant composition and fuel ignition quality. Their study suggests that C_{16}–C_{18} n-alkanes are adequate surrogates for capturing the ignition characteristics

of real base oils and fully formulated lubricants. In this work, lubricant oil is represented using the chemistry of n-hexadecane ($C_{16}H_{34}$). Various chemical kinetics models have been developed for $C_{16}H_{34}$, the fuel that defines 100 cetane number or easy ignition in diesel engines, making it an ideal choice for the representation of lubricant oil in this work [54–58]. Again, a reduced kinetic model that has good chemical representation of $C_{16}H_{34}$ was needed to minimize computational cost.

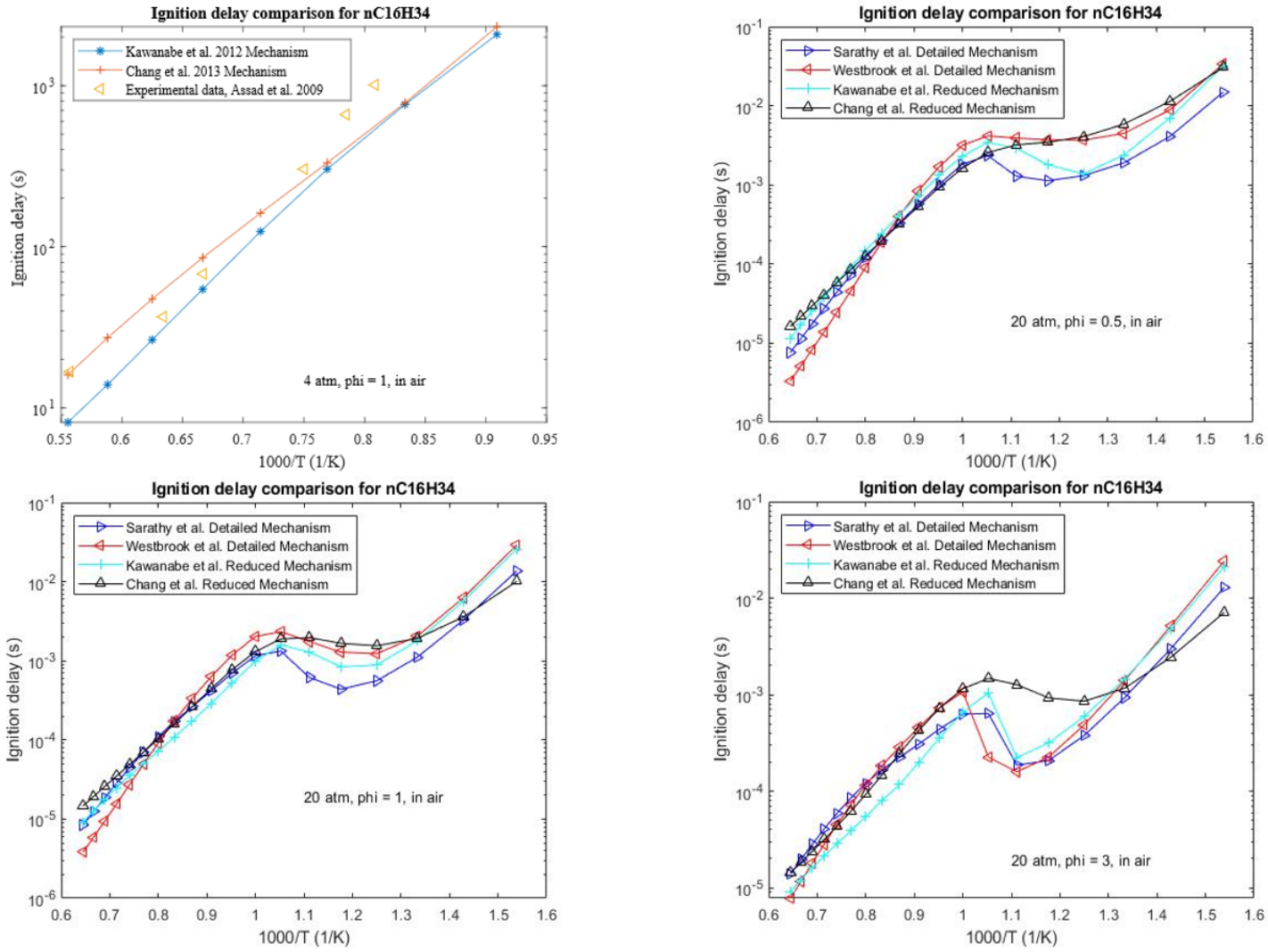

Figure 2.3: Ignition delay comparison conducted by the author for $C_{16}H_{34}$ with detailed kinetic models from Sarathy et al.[49, 59] and Westbrook et al. [53], as well as experimental shock tube data from Assad et al. [60]

Kawanabe et al. [61] and Chang et al. [62] both developed kinetic models with compact sizes intended for integration into CFD simulations. The Kawanabe et al. model consists of 59 species and 96 reactions, and they used it with the CONVERGE CFD solver to simulate the ignition process of a diesel spray under high pressure and temperature conditions. This kinetic model was validated against detailed kinetic models in the literature for ignition delays, as well as temporal change of chemical species for the auto-ignition process, and good agreement was found. Chang et al. [62] built their model using a decoupling methodology. This kinetic model contains 36 species and 128 reactions and was validated against experimental data in a shock tube, jet-stirred reactor, variable pressure flow reactor, counter flow flame under wide ranges of pressure (up to 80 atm), equivalence ratio (0.5–2.0), and temperature (including low-temperature, NTC, and high-temperature regimes).

Table 2.2: Reaction system for sub-mechanism of $C_{16}H_{34}$ [61].

N	Reactions	A	n	E
1	C16H34 + O2 = C16H33 +HO2	1.0×10^{16}	0	46000
	Rev/	1.0×10^{12}	0	0
2	C16H33 + O2 = C16H33O2	1.0×10^{12}	0	0
	Rev/	2.510×10^{13}	0	27400
3	C16H33O2 = C16H32OOH	7.550×10^{10}	0	19000
	Rev/	5.0×10^{10}	0	11000
4	C16H32OOH + O2 = O2C16H32OOH	6.320×10^{11}	0	0
	Rev/	5.020×10^{13}	0	27400
5	O2C16H32OOH => C16KET + OH	2.0×10^{10}	0	17000
6	C16KET => C14H29CO + CH2O + OH	1.990×10^{15}	0	43000
7	C14H29CO + O2 => C14H28 +CO + HO2	3.160×10^{13}	0	10000
8	C14H28 => C3H6 + C3H6 + C3H6 + C3H6 + C2H4	3.0×10^{10}	0	0
9	C14H28 => C7H15 + C3H6 + C2H4 + C2H3	3.160×10^{13}	0	10000
10	C16H34 + OH => C16H33 + H2O	8.0×10^{14}	0	3000
11	C16H33 + O2 = C16H32 + HO2	4.040×10^{11}	0	6000
	Rev/	4.740×10^{11}	0	19500
12	C16H32 + O2 => C14H29 + CH2O + HCO	3.160×10^{13}	0	10000
13	C16H34 + HO2 = C16H33 + H2O2	2.0×10^{13}	0	16950
14	C16H33 => C14H29 + C2H4	4.0×10^{11}	0	28810
15	C14H29 => C3H6 + C3H6 + C3H6 + C3H6 + C2H5	2.138×10^{15}	-0.42	27010

As Figure 2.3 shows, both reduced models agree well with the detailed models of Sarathy et al. [49, 59] and Westbrook et al. [53] for lean and stoichiometric conditions. However, for rich mixtures, the skeletal model of Chang et al. [62] fails to predict the negative temperature coefficient (NTC) behavior of $C_{16}H_{34}$. Nevertheless, comparing simulated results with experimental shock-tube data from Assad et al. shows that both reduced model match trends Ill [60]. Sarathy et al. and Westbrook et al. were challenged by the lack of validation data for fuels with more than 10 C atoms in their kinetic modeling study of n-alkane combustion [49, 53]. They deduced this unavailability of experimental data from the very low vapor pressures of these large hydrocarbon fuels, making well-characterized gas-phase experiments difficult. However, by examining results from the work of Shen et al. and Haylett et al. published subsequently which showed excellent agreement with data from aerosol shock tube studies using modeling predictions from Westbrook et al. model, Sarathy et al. concluded that the systematic extensions of the rule-based kinetic mechanisms from smaller molecules, for which validation data was available, to larger fuels with the same struture, where data were not yet available, could be made with some confidence [63, 64]. Table 2.2 shows the sub-mechanism for $C_{16}H_{34}$ from the work of Kawanabe et al. that was incorporated in this work. Here, the rate coefficients are expressed by the empirical Arrhenius form:

$$k(T) = AT^n \exp\left(-E_A/R_uT\right) \tag{2.1}$$

where A, E_A, n are the three empirical parameters, representing the pre-exponential factor, activation energy, and a constant, respectively [65].

Figure 2.4 shows additional validation of the Kawanabe et al. model that I performed using experimental jet-stirred reactor (JSR) measurements [54]. The model accurately reproduces O_2 consumption at all equivalence ratios, and shows satisfactory agreement for the formation of CH_2O, CH_4, CO, and C_3H_6. However, with the simplified C_2–C_3 and $H_2/CO/C_1$ chemistry implemented in the model, predictions for concentrations of CO_2, H_2, and C_2H_4 (not shown in the figure) were underestimated at the lower bound of the temperature range. $C_{16}H_{34}$ consumption was well predicted, but a slight deviation was observed for temperatures above 1050 K in all cases. This leaves room for further improvement and validation as the researchers continue to develop the kinetic model.

Ultimately, due to its overall performance, the reduced chemical kinetics model for $C_{16}H_{34}$

of Kawanabe et al. [61] was chosen to represent the chemistry of lubricant base oil in the combined model.

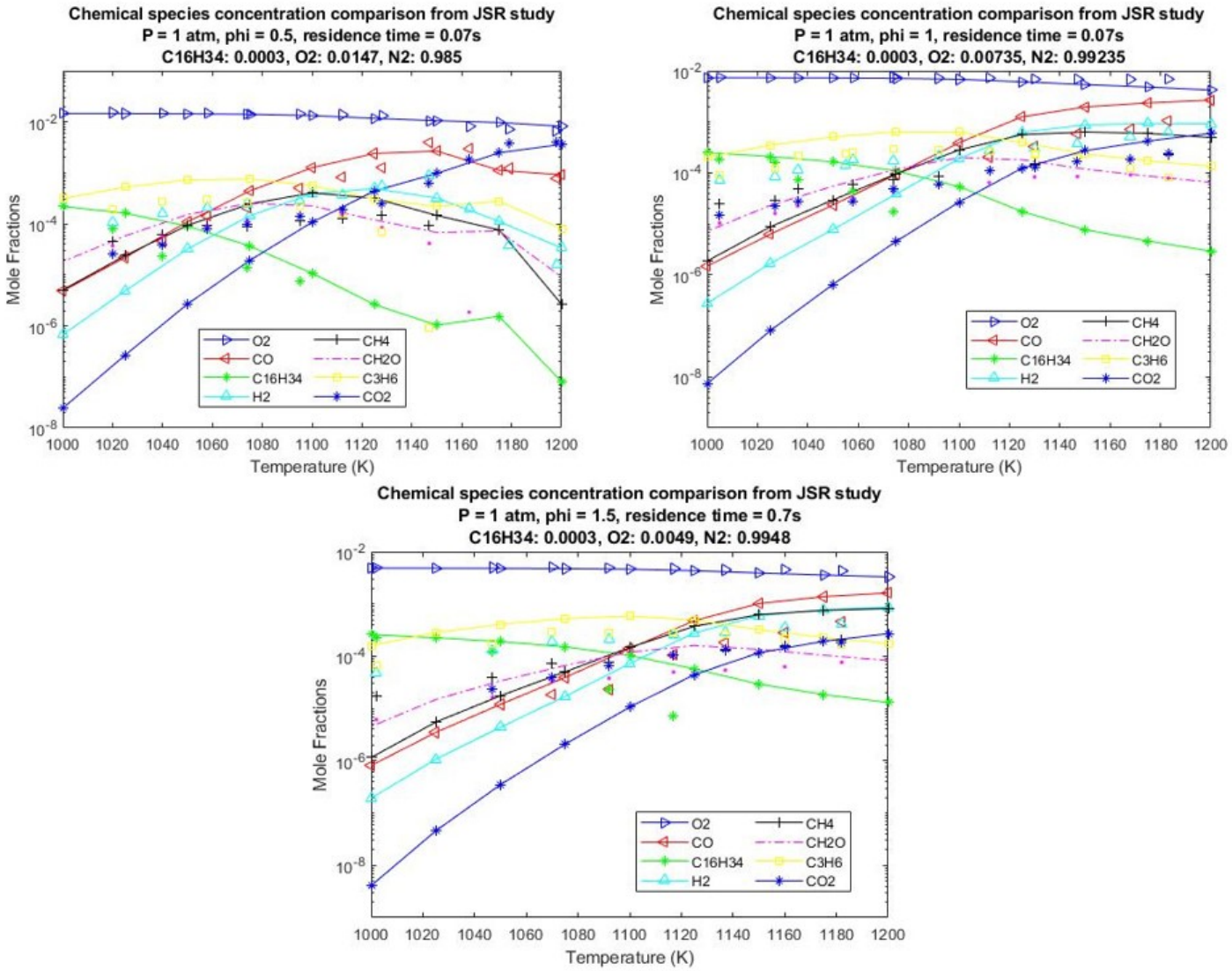

Figure 2.4: Jet-stirred reactor chemical species concentrations comparison for $C_{16}H_{34}$, conducted by the author using the kinetic model from Kawanabe et al. [61].

2.2.3 Oil Additive Package

Various experimental studies in the literature report the effects of different additives within the formulation of lubricant oil. While including certain compounds, such as Ca [35], Fe [33], Cu [33], Na [36] can enhance the frequency of super-knock, the addition of others, like MoDTC [34], ZnDTP [17], Mg [66], K [37], and Li [37] can help prevent super-knock from occuring in GDI engines. Therefore, this work requires an additive package to effectively model LSPI.

Table 2.3: Reactions of Na species, units are in cm, mol, s, and kcal [67].

N	Reactions	A	n	E
1	NaOH + H -> Na + H2O	1.0×10^{13}	0	1.97
2	NaO2 + H -> NaOH + O	1.0×10^{14}	0	0
3	NaO2 + H -> NaO + OH	5.0×10^{13}	0	0
4	NaO2 + H -> HO2 + Na	2.0×10^{14}	0	0
5	NaO2 + O -> NaO + O2	1.0×10^{14}	0	0
6	NaO2 + CO -> NaO + CO2	1.0×10^{14}	0	0
7	NaO2 + OH -> NaOH + O2	2.0×10^{14}	0	0
8	NaO + H -> Na + OH	2.0×10^{14}	0	0
9	NaO + O -> Na + O2	2.2×10^{14}	0	0
10	NaO + OH -> NaOH + O	2.0×10^{13}	0	0
11	NaO + OH -> Na + HO2	3.0×10^{13}	0	0
12	NaO + HO2 -> NaOH + O2	5.0×10^{13}	0	0
13	NaO + HO2 -> NaO2 + OH	5.0×10^{13}	0	0
14	NaO + H2 -> NaOH + H	1.6×10^{13}	0	0
15	NaO + H2 -> Na + H2O	3.1×10^{12}	0	0
16	NaO + H2O -> NaOH + NH2	1.3×10^{13}	0	0
17	NaO + NO -> Na + NO2	9.0×10^{13}	0	0
18	NaO + NH3 -> NaOH + NH2	5.0×10^{13}	0	0
19	NaO + CO -> Na + CO2	1.0×10^{14}	0	0
20	Na + O2 + M -> NaO2 + M	1.7×10^{21}	-1.3	0
21	Na + OH + M -> NaOH + M	1.8×10^{21}	-1	0
22	Na + HO2 -> NaOH + O	1.0×10^{14}	0	0
23	Na + N2O -> NaO + N2	1.7×10^{14}	0	3.16

Kinetic models for metal-containing additives have been developed and used in various modeling efforts. Perry and Miller [68] developed Na−O−H chemistry in an attempt

to investigate the feasibility of using NaOH to control N_2O emissions from combustion sources, which was then used by Zamansky et al. [69, 70] to study sodium species' effect in promoting the selective non-catalytic reduction process. The sub-mechanism for Na-containing species was also used by Lissianski et al. [67] in their investigation into the effects of metal-containing additives on NO_x reduction in combustion and reburning. Lissianski et al. combined the mechanism of Na_2CO_3 decomposition and reactions of Na-containing species to describe the injection of Na_2CO_3 in their model of the reburning process. The sub-mechanism for Na-containing species from the work of Lissianski et al. was included in this work to represent the chemistry of sodium constituents in lubricant oil composition. Table 2.3 details the reactions and rate coefficients in the Arrhenius form of this sub-mechanism.

Table 2.4: Reaction system for sub-mechanism of K/H/O/Cl/S [71, 72].

N	Reactions	A	n	E
1	K + SO2 (+M) = KSO2 (+M)	3.7×10^{14}	0	0
	Low-pressure limit	5.2×10^{23}	-1.50	0
2	K + SO3 (+M) = KSO3 (+M)	3.7×10^{14}	0	0
	Low-pressure limit	4.7×10^{34}	-4.90	0
3	K + SO3 = KO + SO2	1.0×10^{14}	0	7840
4	KO + SO2 (+M) = KSO3 (+M)	3.7×10^{14}	0	0
	Low-pressure limit	5.2×10^{23}	-1.50	0
5	KOH + SO3 (+M) = KHSO4 (+M)	1.0×10^{14}	0	0
	Low-pressure limit	2.6×10^{42}	-7.6	0
6	KSO2 + O = KO + SO2	1.3×10^{13}	0	0
7	KSO2 + OH = KOH + SO2	2.0×10^{13}	0	0
8	KSO2 + KO2 = K2SO4	1.0×10^{14}	0	0
9	KSO3 + O = KO + SO3	1.3×10^{13}	0	0
10	KSO3 + OH = KOH + SO3	2.0×10^{13}	0	0
11	KSO3 + KO = K2SO4	1.0×10^{14}	0	0
12	KHSO4 + KOH = K2SO4 + H2O	1.0×10^{14}	0	0
13	KHSO4 + KCl = K2SO4 + HCl	1.0×10^{14}	0	0
14	KCl + SO3 (+M) = KSO3Cl (+M)	1.0×10^{14}	0	0
	Low-pressure limit	1.9×10^{41}	-7.80	0
15	KSO3Cl + OH = KHSO4 + Cl	1.0×10^{14}	-0.42	0
16	KSO3Cl + H2O = KHSO4 + HCl	1.0×10^{14}	-0.42	0
17	KSO3Cl + KOH = K2SO4 + HCl	1.0×10^{14}	-0.42	0

A chemical kinetic sub-model for potassium (K), another additive of interest in LSPI research, was also incorporated in the overall model to bolster the additive package. The potassium chemistry was taken from the work of Hindiyarti et al. [72], who studied alkali sulfate aerosol formation during biomass combustion. Based on the work proposed earlier by Glarborg and Marshall [71], this model contains subsets for H_2/O_2, chlorine, sulfur, and potassium chemistry, as well as the interactions between these subsets. Table 2.4 highlights the K/H/O/Cl/S subsystem from the work of Glarborg and Marshall that was incorporated in the final reduced chemical mechanism. Interested readers are directed to Appendix 5 for full details of this chemical kinetics model, as well as rate coefficients of the reactions from other subsystems in the work of Glarborg, Marshall, and Hindiyarti et al. A chemical kinetics model for Ca, an oil additive of very high interest in the research body of LSPI, was also considered to be part of this work's additive package. However, due to the lack of research and development in regard to Ca, no kinetics model of said additive is currently available in the literature. This leaves room for further work as the researchers continue to develop and validate kinetics models for super-knock research.
In summary, a chemical kinetic model was developed here specifically for computational studies of LSPI in GDI engines. Sub-models of PRFs and $C_{16}H_{34}$ were included as surrogates for gasoline and lubricant base oil, respectively. An additive package, currently including chemical reactions of sodium and potassium-containing species, is also available in the kinetic model to investigate the included compounds' effect on super-knock frequency. The full version of this reduced chemical kinetics model can be found at the following repository [73].

Chapter 3: Computational Fluid Dynamics Implementation

Computational fluid dynamics is the analysis of systems involving fluid flow, heat transfer, and associated phenomena such as chemical reactions by means of computer-based simulation. A powerful technique, the application of CFD spans a wide range of industrial and non-industrial application areas from analysis of blood flows through arteries and veins to aerodynamics of aircraft and vehicles [74]. In this work, the commercial CFD software CONVERGE was used to implemented the developed reduced chemical kinetics model from Chapter 2 for the investigation of low-speed pre-ignition phenomenon. In this chapter, a brief overview of the governing equations and models used in this CFD framework is provided. A complete description of these models is outside the scope of this thesis and interested readers are directed to the corresponding references for additional information.

3.1 General Transport and Governing Equations

The dynamics of fluid flow are governed by equations that describe the conservation of mass, momentum, and energy [75]. The unsteady, three-dimensional mass conservation at a point in a compressible fluid is given as:

$$\frac{\partial \rho}{\partial t} + \frac{\partial \rho u_i}{\partial x_i} = S \tag{3.1}$$

whereas the conservation of momentum equation is given as the following:

$$\frac{\partial \rho u_i}{\partial t} + \frac{\partial \rho u_i u_j}{\partial x_j} = -\frac{\partial P}{\partial x_i} + \frac{\partial \sigma_{ij}}{\partial j} + S_i \tag{3.2}$$

in which the viscous stress tensor is given by:

$$\sigma_{ij} = \mu \left(\frac{\partial u_i}{\partial x_j} + \frac{\partial u_j}{\partial x_i} \right) + \left(\mu' - \frac{2}{3}\mu \right) \left(\frac{\partial u_k}{\partial x_k} \delta_{ij} \right) \tag{3.3}$$

In the above equations, u is velocity, is density, S is the source term, P is pressure, μ is viscosity, $\mu^{'}$ is the dilatational viscosity, and δ_{ij} is the Kronecker delta. Finally, the energy equation is given by:

$$\frac{\partial \rho e}{\partial t} + \frac{\partial u_j \rho e}{\partial x_j} = -P\frac{\partial u_i}{\partial x_j} + \sigma_{ij}\frac{\partial u_i}{\partial x_j} + \frac{\partial}{\partial x_j}\left(K\frac{\partial T}{\partial x_j}\right) + \frac{\partial}{\partial x_j}\left(\rho D \sum_m h_m \frac{\partial Y_m}{\partial x_j}\right) + S \quad (3.4)$$

where ρ is density, Y_m is the mass fraction of species m, D is the mass diffusion coefficient, S is the source term, P is the pressure, e is the specific internal energy, K is the conductivity, h_m is the species enthalpy, σ_{ij} is the stress tensor, and T is temperature. If a turbulence model is activated, CONVERGE replaces the conductivity with the turbulent conductivity, which is given by:

$$K_t = K + c_p \frac{\mu_t}{\mathrm{Pr}_t} \quad (3.5)$$

where $Pr_t = \frac{c_p \mu_t}{k_t}$ is the turbulent Prandtl number and μ_t is the turbulent viscosity.

3.2 Turbulence Modeling

All flows encountered in engineering practice, ranging from two-dimensional jets, wakes, and flat plate boundary layers to more complicated three-dimensional ones, become unstable above a certain Reynolds number [76]. At higher Reynolds numbers, flows are observed to become turbulent. Turbulence significantly increases the rate of mixing of momentum, energy, and species, as well as causes the appearance in the flow of eddies with a wide range of length and time scales that interact in a dynamically complex way. Therefore, having a turbulence model is necessary to attain accurate CFD simulation results.

Substantial amount of research, dedicated to the development of numerical methods to capture the important effects due to turbulence in different engineer applications, have been found in the literature [74]. The published methods can be categorized into three groups:

- **Turbulence models for Reynolds-Averaged Navier-Stokes (RANS) equations**: where the focus is on the mean flow and the effects of turbulence on mean flow properties. The Navier-Stokes equations are time averaged and the appear-

ance of the extra terms from time-averaged are due to the interactions between various turbulent fluctuations. In terms of required computing resources, modest cost is needed to acquire reasonably accurate flow computations, which makes this approach attractive for engineering flow calculations in the literature.

- **Large Eddy Simulation (LES)**: an intermediate form of turbulence calculations, in which the behaviour of larger eddies are tracked. The approach involves space filtering of the unsteady Navier-Stokes equations prior to computations, which passes the larger eddies and rejects the smaller eddies. Unsteady flow equations must be solved, which requires larger demand for computing resources comparing to RANS.

- **Direct Numerical Simulation (DNS)**: where all turbulent velocity fluctuations and the mean flow are computed. Spatial grids are sufficiently fine when solving the unsteady Navier-Stokes equations, resulting in capability to resolve the Kolmogorov length scales. As a result, computational cost for this method is extremely high, and therefore this approach is not used for industrial applications.

Within CONVERGE CFD, three turbulence modeling options are available, namely Reynolds-Averaged Navier-Stokes (RANS) [77], Detached Eddy Simulation (DES) [78], and Large Eddy Simulation (LES) [79]. In this work, the RANS approach with RNG (Renormalization Group) $k-\epsilon$ turbulence model was utilized to model the effect of turbulence in GDI engine. A two-equation RANS model, the flow variables are decomposed into an ensemble mean and a fluctuation term as follows:

$$u_i \quad = \quad \overline{u}_i \quad + \quad u_i' \tag{3.6}$$

The RANS transport equations and averaging are then obtained from substituting the above RANS decomposition into the Navier-Stokes equations, which yields the compressible RANS equations for mass and momentum transport as follows:

$$\frac{\partial \overline{\rho}}{\partial t} + \frac{\partial \overline{\rho}\tilde{u}_j}{\partial x_j} = 0 \tag{3.7}$$

$$\frac{\partial \overline{\rho}\tilde{u}_i}{\partial t} + \frac{\partial \overline{\rho}\tilde{u}_i\tilde{u}_j}{\partial x_j} = -\frac{\partial \overline{P}}{\partial x_i} + \frac{\partial}{\partial x_j}\left[\mu\left(\frac{\partial \widetilde{u}_i}{\partial x_j} + \frac{\partial \widetilde{u}_j}{\partial x_i}\right) - \frac{2}{3}\mu\frac{\partial \widetilde{u}_k}{\partial x_k}\delta_{ij}\right] + \frac{\partial}{\partial x_j}\left(-\overline{\rho}\widetilde{u_i'u_j'}\right) \tag{3.8}$$

where the Favre average, $\sim$, is defined for velocity as:

$$\widetilde{u}_i = \frac{\overline{\rho u}_i}{\overline{\rho}} \tag{3.9}$$

Additional terms from the ensamble averaging of the equations, namely the Reynolds stresses that represent the effects of turbulence, is given by:

$$\tau_{ij|} = -\overline{\rho u_i' u_j'} \tag{3.10}$$

3.3 Combustion Modeling

CONVERGE CFD includes several combustion models for both premixed and non-premixed combustion. Since the combustion process within GDI engines is non-premixed, two different modeling methods, via the use of the SAGE Detailed Chemical Kinetics Solver as well as a combination of the Shell ignition model and the Characteristic Time Combustion model, were under consideration for combustion modeling in this work [80, 81]. While the latter method is relatively computationally inexpensive, the former method considers much of the chemistry taking place in combustion applications, resulting in longer runtime but greatly enhanced accuracy from the simulations [75]. Therefore, the SAGE solver was chosen to model the combustion process in this body of work.

Developed by Senecal and his colleagues, the SAGE detailed chemical kinetics solver allows for any number of chemical species and reactions to be modeled via a set of CHEMKIN-formatted input files [81]. When a chemical reaction mechanism is specified within CONVERGE CFD, the SAGE solver calculates the reaction rates for each elementary reaction contained in the mechanism, while the CFD solver solves the transport equations. In SAGE, a multi-step chemical reaction mechanism is written in the following form:

$$\sum_{m=1}^{M} \nu'_{m,r} \chi_m \Leftrightarrow \sum_{m=1}^{M} \nu''_{m,r} \chi_m \qquad \text{for } r = 1, 2, \ldots R \tag{3.11}$$

where $v'_{m,r}$ and $v''_{m,r}$ are the stoichiometric coefficients for the reactants and products, respectively, for species m and reaction r; R is the total number of reactions; and χ_m is

the chemical symbol for species m . The net production rate of species m is given by:

$$\dot{\omega}_m = \sum_{i=1}^{R} \nu_{m,q} q_r \text{ for } m = 1, 2, \ldots M \tag{3.12}$$

where M is the total number of species and

$$\nu_{m,r} = \nu''_{m,r} - \nu'_{m,r} \tag{3.13}$$

The rate-of-progress parameter q_r for the r^{th} reaction is:

$$q_r = k_{fr} \prod_{m=1}^{M} [X_m]^{\nu'_{m,r}} - k_{rr} \prod_{m=1}^{M} [X_m]^{\nu''_{m,r}} \tag{3.14}$$

where $[X_m]$ is the molar concentration of species m, and k_{fr} and k_{rr} are the forward and reserve rate coefficients for reaction r. Here the forward rate coefficient is expressed by the Arrhenius form as:

$$k_{fr} = A_r T^{b_r} e^{(-E_r/R_u T)} \tag{3.15}$$

where A_r is the pre-exponential factor, b_r is the temperature exponent, E_r is the activation energy, and R_n is the universal gas constant. Additionally, the reverse rate coefficient can b calcualted from the equilibrium coefficient K_{cr} as:

$$k_n = \frac{k_{ft}}{K_\sigma} \tag{3.16}$$

where the equilibrium coefficient K_{cr} is determined from the thermodynamic properties and is given by:

$$K_{cr} = K_{pr} \left(\frac{P_{atm}}{RT} \right)^{\sum_{m=1}^{M} v_{mr}} \tag{3.17}$$

where P_{atm} is the atmospheric pressure, R is the gas constant, and T is the temperature. The equilibrium constant K_{pr} is obtained via:

$$K_{pr} = \exp\left(\frac{\Delta S_r^0}{R} - \frac{\Delta H_r^0}{RT} \right) \tag{3.18}$$

The Δ refers to the change that occurs in passing completely from reactants to products in the r'^n reaction, specifically,

$$\begin{aligned} \frac{\Delta S_r^0}{R} &= \sum_{m=1}^{M} \nu_{mr} \frac{S_m^0}{R} \\ \frac{\Delta H_r^0}{RT} &= \sum_{m=1}^{M} \nu_{mr} \frac{H_m^0}{RT} \end{aligned} \tag{3.19}$$

3.4 Spray Modeling

3.4.1 Droplet Breakup Model

Several spray breakup models are present in CONVERGE CFD, including the Kelvin-Helmholz (KH) and Rayleigh-Taylor (RT) instability mechanisms [82, 83], the LISA sheet breakup model [84], and the Taylor Analogy Breakup (TAB) drop breakup model [85]. In this work, the primary injection size distribution is represented by the Rosin-Rammler distribution [86]. Otherwise known as the "two-parameter Weibull distribution", this distribution is frequently used to model droplet size distributions and was used to model the initial droplet size distribution. The cumulative probability function for the Rosin-Rammler distribution is given by:

$$\tilde{R}(r) = 1 - \exp\left[-\zeta^4\right], \quad 0 < \zeta < \zeta_{\max} \tag{3.20}$$

where $\zeta = \frac{r}{\overline{r}}$. Here, q is an empirical constant, and $\overline{r} = \Gamma\left(1 - q^{-1}\right) r_{32}$. Γ is the gamma function and r_{32} is the Sauter mean radius. Once a value of ζ is selected, the injected drop radius is determined via the following equation:

$$r = \overline{r}\zeta = \Gamma\left(1 - q^{-1}\right) r_{32}\zeta \tag{3.21}$$

The secondary breakup process is often modeled using the hybrid Kelvin-Helmholtz wave model and Rayleigh-Taylor model. Described in details in the work of Reitz and Bracco, The KH model is based on liquid jet stability analysis, and examines the stability of the surface of a cylindrical liquid jet to perturbations using a first order theory [82]. The viscous liquid jet with velocity U is injected into a stagnant, incompressible, inviscid gas of desity ρ_g. An arbitrary infinitesimal axisymmetric surface displacement is imposed to

the initially steady surface in the form of the following equation:

$$\eta = \eta_o e^{ikz+\omega t} \tag{3.22}$$

Additionally, a dispersion equation, one that includes the physical and dynamical parameters of the liquid jet and surrounding gas, is derived from the linearized hydrodynamical equations. This dispersion equation is given as:

$$\begin{aligned} &\omega_{KH}^2 + 2v_l k_{KH}^2 \omega_{KH} \left[\frac{I_1'(k_{KH} r_p)}{I_0(k_{KH} r_p)} - \frac{2k_{KH} L}{k_{KH}^2 + L^2} \frac{I_1(k_{KH} r_p)}{I_0(k_{KH} r_p)} \frac{I_1'(L r_p)}{I_1(L r_p)} \right] = \\ &\frac{\sigma k_{KH}}{\rho_l r_p^2} \left(1 - k_{KH}^2 r_p^2\right) \left(\frac{L^2 - r_p^2}{L^2 + r_p^2} \right) \frac{I_1(k_{KH} r_p)}{I_0(k_{KH} r_p)} + \\ &\frac{\rho_g}{\rho_l} \left(U - i \frac{\omega_{KH}}{k_{KH}} \right)^2 \left(\frac{L^2 - r_p^2}{L^2 + r_p^2} \right) I_0 \left(k_{KH} r_p \right) \frac{K_0(k_{KH} r_p)}{K_1(k_{KH} r_p)} \end{aligned} \tag{3.23}$$

where K_0 and K_1 are modified Bessel functions of the second kind. In the KH model, the initial parcel diameters are set equal to the nozzle hole diameter d_0 and the atomization process of the relatively large injected blobs is modeled using the stability analysis for liquid jets. Parent parcel breaks up to form new droplets, which is determined by:

$$r_c = B_o \Lambda_{KH} \tag{3.24}$$

where B_0 is a model constant typically set to 0.61 based on the work of Reitz et al., and Λ_{KH} is given by:

$$\frac{\Lambda_{KH}}{r_p} = 9.02 \frac{\left(1 + 0.45 Z_l^{0.5}\right) \left(1 + 0.4 T^{0.7}\right)}{\left(1 + 0.87 We_g^{1.67}\right)^{0.6}} \tag{3.25}$$

Furthermore, the rate of change in the radius of the parent droplet parcel is described by the following relationship:

$$\frac{dr_p}{dt} = -\frac{(r_p - r_c)}{\tau_{kH}}, \quad (r_c \leq r_p) \tag{3.26}$$

where the breakup time τ_{KH} is given by:

$$\tau_{KH} = \frac{3.726 B_1 r_p}{\Lambda_{KH} \Omega_{KH}} \tag{3.27}$$

$$\Omega_{KH}\left[\frac{\rho_l r_p^3}{\sigma}\right]^{05} = \frac{(0.34 + 0.38We_8^{15})}{(1+Z_1)(1+1.4T^{0.6})} \tag{3.28}$$

Additional droplet breakup is represented by the Rayleigh-Taylor instability model, which is used in conjunction with the KH model to predict instabilities on the surface of the droplet that grow until a certain characteristic breakup time when the drop finally breaks up [83]. Based on wave instability theory. the unstable RT waves are thought to occur due to the rapid deceleration of the drops from the magnitude of the drag force, which is given as:

$$|F_{D,i}| = M_d |a_i| = M_d \frac{3}{8} C_D \frac{\rho_g |U_i|^2}{\rho_l r_o} \tag{3.29}$$

where $|a_i|$ is the deceleration of the drop, m_d is the mass of the drop, and C_D is the drag coefficient. Typical implementations of the RT breakup model ignore both gas and liquid viscosity, yielding the frequency of its fastest growing wave and corresponding wavelength in the form of:

$$\Lambda_{RT} = 2\pi\sqrt{\frac{3\sigma}{a(\rho_l - \rho_g)}} \tag{3.30}$$

$$\Omega_{RT} = \sqrt{\frac{2}{3\sqrt{3\sigma}} \frac{[a(\rho_l - \rho_g)]^{3/2}}{\rho_l + \rho_g}} \tag{3.31}$$

The Kelvin-Helmholz Rayleigh-Taylor (KH-RT) breakup length model, resulting from running the two aforementioned models concurrenty, was implemented in this work. When activated, the model specifies an intact core or breakup length L_b of the form:

$$L_b = C_{Bl}\sqrt{\frac{\rho_l}{\rho_g}} d_0 \tag{3.32}$$

3.4.2 Droplet Collision Model

Within CONVERGE CFD, two droplet collision models are available for incorporation, namely the O'Rourke model and the No Time Counter method from the work of Schmidt and Rutland [87, 88]. While the O'Rourke collision and coalescence model is designed to estimate the number of droplet collisions and their outcomes in a relatively computationally efficient manner, the NTC method is based on techniques used in gas dynamics for Direct Simulation Monte Carlo calculations, and has been shown to be faster and

more accurate than the O'Rourke model under certain conditions. In this simulation framework, the NTC numerical scheme was chosen to model collision of droplets entering the combustion chamber via direct injection.

The NTC model involves stochastic sub-sampling of the parcels within each cell, which results in much faster collision calculations. Comparing to the O'Rourke numerical scheme, which incurs an additional computational cost that increase with the square of the number of parcels, the NTC method has a linear cost, and produces more accurate results via its repeated sampling. Derived from the basic probability model for stachastic collision, the model requires that the cell size is sufficiently small such that spatial variations in spray quantities can be neglected. The NTC method details the expected number of collisions in a cell over a time interval of Δt as:

$$M_{coll} = \frac{1}{2} \sum_{i=1}^{N} \sum_{j=1}^{N} \frac{V_{i,j} \sigma_{i,j} \Delta t}{\forall} \tag{3.33}$$

where the factor of one-half comes from symmetry. If the individual droplets are grouped into parcels having identical properties, then the double summation becomes:

$$M_{coll} = \frac{1}{2} \sum_{i=1}^{N_p} q_i \sum_{j=1}^{N_p} q_j \frac{V_{i,j} \sigma_{i,j} \Delta t}{\forall} \tag{3.34}$$

where N_p is the number of parcels in the cell and q is the number of droplets in a parcel. Additional modification can be made by pulling a constant factor outside of the summation, reducing the computational cost, yielding:

$$M_{coll} = \frac{(qV\sigma)_{\max} \Delta t}{2\forall} \sum_{i=1}^{N_p} q_i \sum_{j=1}^{N_p} \frac{q_j V_{i,j} \sigma_{i,j}}{(qV\sigma)_{\max}} \tag{3.35}$$

Further details on the derivation of this method can be found in the work of Schmidt and Rutland [88]. The result, the final expression of the NTC method for application to parcels representing varying numbers of drops, is as follows:

$$M_{coll} = \sum_{i=1}^{\sqrt{M_{cand}}} q_i \sum_{j=1}^{\sqrt{M_{cand}}} \frac{q_j V_{i,j} \sigma_{i,j}}{(qV\sigma)_{\max}} \tag{3.36}$$

where $M_{cand} = \frac{N_p^2 (qV\sigma)_{\max} \Delta t}{2\forall}$.
Additionally, the Post Collision Outcomes model is used in conjunction with the NTC method to account for grazing collision, coalescence outcomes, stretching separation and reflexive separation [89]. In this model, the collision Weber number is first compared with a bouncing parameter given by:

$$We_{\text{Bource}} = \frac{\Delta_p \left(1 + \Delta_p^2\right) (4\phi' - 12)}{\chi_1 [\cos(\arcsin B)]^2} \tag{3.37}$$

where $\Delta_p = \frac{r_1}{r_2}$ with $r_1 < r_2$. The model compares between the two quantities, We_{Bource} and We_{Coll}, and two scenarios are taken into consideration. If $We_{\text{Bource}} > 2We_{\text{Coll}}$, it is assumed that the two drops bounce, and the post bounce velocies are calculated accordingly:

$$v_{i,1} = \frac{m_1 v_{i,1} + m_2 v_{i,2} + m_2 \left(v_{i,1} - v_{i,2}\right)}{m_1 + m_2} \tag{3.38}$$

$$v_{i,2} = \frac{m_1 v_{i,1} + m_2 v_{i,2} + m_1 \left(v_{i,2} - v_{i,1}\right)}{m_1 + m_2} \tag{3.39}$$

Whereas if $2We_{coll} \geq We_{bounce}$, then either permanent coalescence, stretching separation, or reflexive separation take place. Two other criteria are checked to determined if a separation has occurred. Possibility of reflexive separation is also taken into account if:

$$2We_{coll} > 3 \left[7 \left(1 + \Delta_p^3\right)^{2/3} - 4 \left(1 + \Delta_p^2\right)\right] \frac{\Delta_p \left(1 + \Delta_p^3\right)^2}{\Delta_p^6 \eta_1 + \eta_2} \tag{3.40}$$

Interested readers are directed to the correspondign references for additional details of these criteria.

3.4.3 Droplet Evaporation Model

CONVERGE CFD offers vaporization models to determine how the radius of a drop changes over time. Once the liquid spray is injected into the computational domain, a model is needed to convert the liquid into gaseous vapor. In this study, the Frossling correlation was used to determine the time rate of change of droplet size [90]. From the

work of Amsden et al., the correlation is given as:

$$\frac{dr_0}{dt} = -\frac{\alpha_{spray}\rho_g D}{2\rho_l r_0} B_d Sh_d \tag{3.41}$$

where α_{spray} is the user-specified sclaing factor for the mass transfer coefficient, and D is the mass diffusivity of liquid vapor in air. The quantity B_d is given as:

$$B_d = \frac{Y_1^* - Y_1}{1 - Y_1^*} \tag{3.42}$$

where Y_1' is the vapor mass fraction at the drop's surface, and Y_1 is the vapor mass fraction. The Sherwood number, Sh_D, is given by:

$$Sh_d = \left(2.0 + 0.6\,\mathrm{Re}_d^{1/2}\,Sc^{1/3}\right)\frac{\ln\left(1+B_d\right)}{B_d} \tag{3.43}$$

where:

$$\mathrm{Re}_d = \frac{\rho_{gas}\left|u_i + u_i' - v_i'\right| d}{\mu_{air}} \tag{3.44}$$

where d is the drop diameter and μ_{air} is the air viscosity which is evaluated at the temperature $\widehat{T}$ given by:

$$\widehat{T} = \frac{T_{gas} + 2T_d}{d} \tag{3.45}$$

where T_{gas} is the gas temperature and T_d is the drop temperature. Additional details on the development of this model can be found in the work of Amsden et al.

3.5 Lubricant Oil Droplet Modeling

The presence of oil droplet in the combustion chamber is carried out using the species source modeling tool in CONVERGE [91]. The compressible form of the species transport equation is given by:

$$\frac{\partial \rho_m}{\partial t} + \frac{\partial \rho_m u_j}{\partial x_j} = \frac{\partial}{\partial x_j}\left(\rho D \frac{\partial Y_j}{\partial x_j}\right) + S_m \tag{3.46}$$

where:

$$\rho_m = Y_m \rho \tag{3.47}$$

In these equations, u is defined as velocity, ρ is density, ρ_m is the density of the species, Y_m is the mass fraction of species m, D is the mass diffusion coefficient, and S_m is the species source term of species m. The molecular mass diffusion coefficient is calculated by:

$$D = \frac{v}{Sc} \tag{3.48}$$

where Sc is the Schmidt number. If a turbulence model has been activated in CONVERGE, the turbulent mass diffusion coefficient is given by:

$$D_t = \frac{v_t}{Sc_t} \tag{3.49}$$

in which Sc_t is the turbulent Schmidt number. The source term is the species equation accounts for evaporation, chemical reactions from combustion, and other sub-models within the simulation.

Chapter 4: Results & Discussion

The developed kinetic model, which includes sub-mechanisms for Na and K, were used to investigate the effect of lubricant oil constituents on super-knock. Ignition delay studies were carried out using Cantera constant volume, zero-dimensional ideal gas reactor. The species time-history of the hydroxyl (OH) radical were tracked to compute the ignition delay in our simulations. Figure 1.5 shows the effect of increasing sodium content in lubricant base oil, which is represented by the chemistry of $C_{16}H_{34}$.

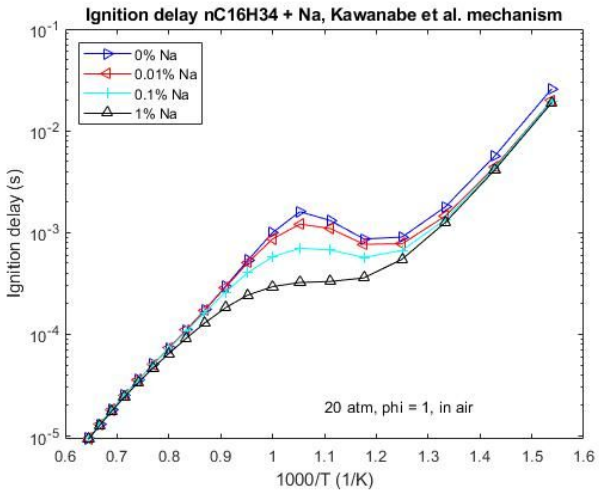

Figure 4.1: Ignition delays for blends of $C_{16}H_{34}$ with varying amounts of Na.

Adding 1% of Na (by volume) to the lubricant oil surrogate ($C_{16}H_{34}$) reduced the ignition delay of the mixture by about 47%. The shortening in ignition delay time indicates higher propensity for pre-ignition, if the Na-containing additive is used in the formulation of engine lubricants. This trend agrees with the experimental study conducted by Kassai et al. [92], who showed that adding Na triggers an increase in normalized super-knock frequency.

An ignition delay study for mixtures of lubricant oil surrogate, $C_{16}H_{34}$, and K-containing additive were also carried out. These results are shown in Figure 4.2. Adding potassium

does not significantly affect the ignition delays of the surrogate lubricant oil mixture, up to the 1% by volume level, in contrast to the effects of adding sodium. However, as the amount of potassium increased to 5% and 10% by vol, a decrease in ignition delay was observed. Nevertheless, such a large amount of additives in the formulation of lubricant oil is not realistic, and is not carried out in industry.

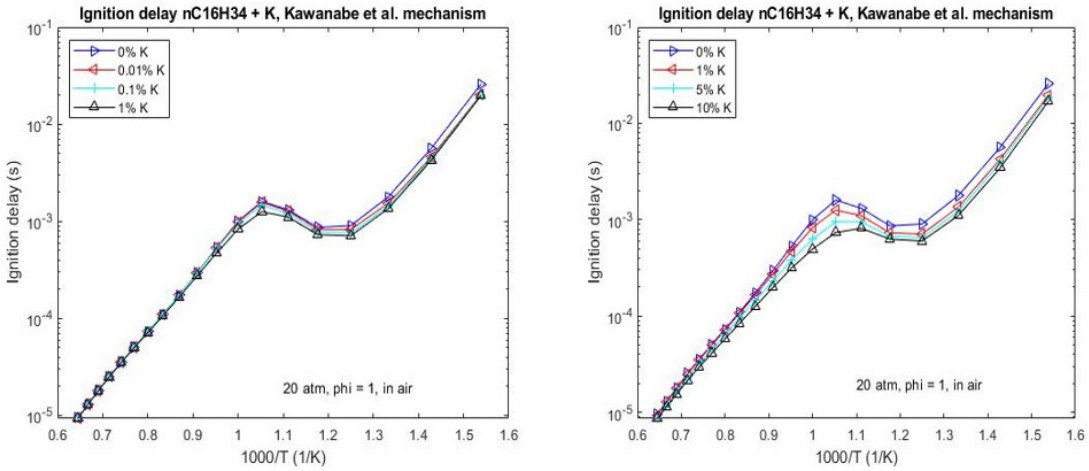

Figure 4.2: Ignition delays for blends of $C_{16}H_{34}$ with varying amounts of K.

These results suggest a neutral or minor preventative effect for pre-ignition/super-knock from K-containing additives in lubricant oils. Although additional experimental data is needed to further verify this trend, the result from this ignition delay study agrees with the report from recent publications for lubricating oil composition to prevent super-knock in GDI engines [37]. In this published work, the addition of at least one K-containing compound from about 300–3500 ppm of metal based on total weight of lubricant oil was reported to reduce LSPI by more than 50% based on normalized super-knock counts per 100,000 engine cycles, with RPM between 500–3000 and BMEP between 10–30 bar.

I also studied the auto-ignition behavior of blends of fuel (represented by iC_8H_{18}) and lubricant oil (represented by $C_{16}H_{34}$) with Na and K to examine the effect of fuel injection on my previous results. Blends of 75% lubricant oil ($C_{16}H_{34}$) and 25% fuel (iC_8H_{18}), by volume, were used, which Qi et al. [20] reported to cause the heaviest knock. I included potassium and sodium in the same proportions as previous studies, ranging from 0%vol oil–1%vol oil. Figure 4.3 shows the results of these simulations.

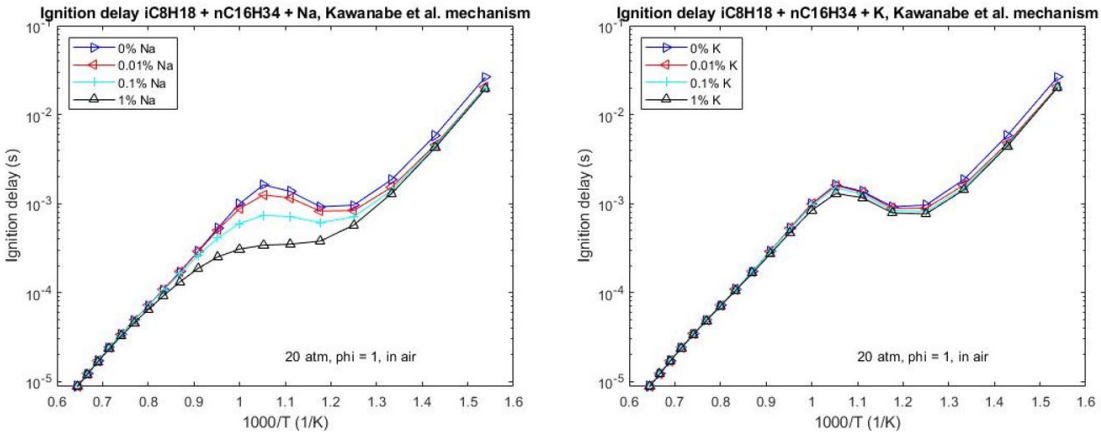

Figure 4.3: Ignition delay for blends of gasoline surrogate (iC_8H_{18}), lubricant oil surrogate ($C_{16}H_{34}$) with addition of Na (left) and K (right).

Table 4.1: CONVERGE GDI engine specifications and operating conditions implemented in this study.

Bore	0.086 (m)
Stroke	0.098 (m)
Connecting rod length	0.1437 (m)
Compression ratio	10
Valves	Two intake and two exhaust valves
Spark time	-15 CAD
Fuel injection time/Duration	-220 CAD/31.1 CAD
RPM	1200
Intake temperature	363 (K)
Intake pressure	101325 (Pa)
Fuel	$C_{18}H_{38}$

I observed similar trends for mixtures of gasoline and lubricant oil with the addition of sodium and potassium as additive constituents. Adding higher amounts of Na (up to 1% vol) to the fuel/oil blend reduces the ignition delay, whereas adding K of the same proportion as Na did not significantly change ignition delay. These results further point to the effect of oil additive constituents on LSPI, in presence of droplet dilution from fuel direct injection.

Next, CONVERGE CFD software was used to implement the developed reduced kinetic

Table 4.2: Input parameters for lubricant oil species source modeling in CONVERGE CFD.

Species	$C_{16}H_{34}$ + Na
Species mass	0.006 (kg)
Temperature	1000 (K)
Velocity	0 (m/s)
Start time	-90 CAD
End time	-60 CAD
Shape and location	Sphere at (x = 0, y = 0, z = -0.05 m)
Radius	0.00045 (m)
Motion	Move with flow

model in order to model the effect of lubricant oil intrusion leading to super-knock occurrence. Specifications of the GDI engine modeled in CONVERGE, as well as the operating conditions are given in Table 4.1 below. Simulations were performed at a compression ratio of 10 and low-speed, high-low conditions where LSPI occurrence is prevalent. A base grid of 4mm was used in all directions with CONVERGE Adaptive Mesh Refinement (AMR) of level 3. This refines the cells locally to achieve a minimum cell size of 0.5mm (minimum cell size = $dx/2^{level}$) to capture the flame front. A cell size of 1mm was embedded in the region covering the cylinder. Near the injector, a cell size of 0.5mm was embedded to better capture spray dynamics. At the spark location, to capture the initial flame kernel growth due to energy sourcing, cells of size 0.125mm were embedded and maintained from -16 CAD to 0 CAD around the spark source location. Different maximum convection CFL values were specified for different regions in the computational domain. For the intake system, max CFL value of 1 was used from intake valve opening to intake valve closing. At all other times, the value of 5 for max CFL number was chosen. Similar decision was made for the cylinder, with max CFL value of 1 from intake valve opening to exhaust valve closing and 5 all other times. In the exhaust system, the max CFL value of 5 was used at all times since the exhaust port needs only to purge the burned gases from the cylinder, and I was not interested in accurately modeling the flow through the exhaust system.

C_8H_{18} was again chosen as surrogate for gasoline to minimize the computational effort, as well as to account for fuel properties effect that could potentially impact results. This was motivated from the defined octane rating of 100 for C_8H_{18}, as specified in test-

ing procedures for Research Octane Number (RON) and Motor Octane Number (MON) discussed in the work of Haywood [24]. By using a gasoline surrogate with the highest rating for anti-knock, the impact of fuel properties within my model in that regard can be minimized, and the focus on lubricant oil effect is unaffected.

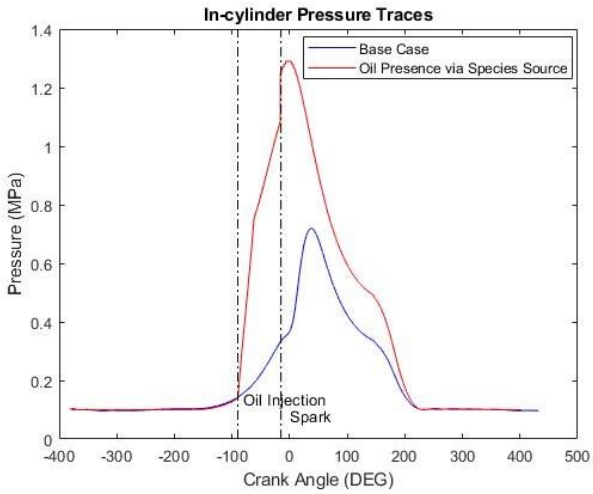

Figure 4.4: In-cylinder pressure trace comparison between base case engine simulation and lubricant oil presence

I performed two different full engine cycle, three dimensional simulated cases in CONVERGE, using the aforementioned engine specification and engine operating conditions. A base case without engine oil intrusion was performed to provide baseline data for comparison with when oil droplets are introduced in the combustion chamber computational domain. The second case implemented the chemistry of $C_{16}H_{34}$ and Na as surrogate for lubricant oil droplets and their constituents. The input parameters for this implementation can be seen in Table 4.2 elow. I selected the location and start/end time of the droplet based on the work of Ali et al., where the effect of timing and location of hot spot on LSPI during pre-ignition were investigated [44]. Their study reported hot spot timing at -90 CAD to show signs of auto-ignition in the end gas. Although the pressure oscillations are not severe at -90 CAD, a pre-ignition event at that specified crank angle or later could lead to LSPI.

I selected the size of the droplet based on the work of Kalghatgi [31]. In his publication, the author argued that a spherical droplet of fuel and oil of a diameter of 100 microns

(0.1 mm) would release around 17 mJ of energy if it were to be completely burned. If all other conditions are satisfied, such a droplet can provide more energy than a typical spark and plausibly set off a flame in a pre-ignition event. I further increased the radius of the droplet in our CFD study, as well as having high input temperature of 1000 K to induce a pre-ignition flame in the domain in addition to immediate initiation of the flame without time delay in the simulation. This high input temperature was also observed to associate with reduction in ignition delay time, as reported in Figure 1.5.

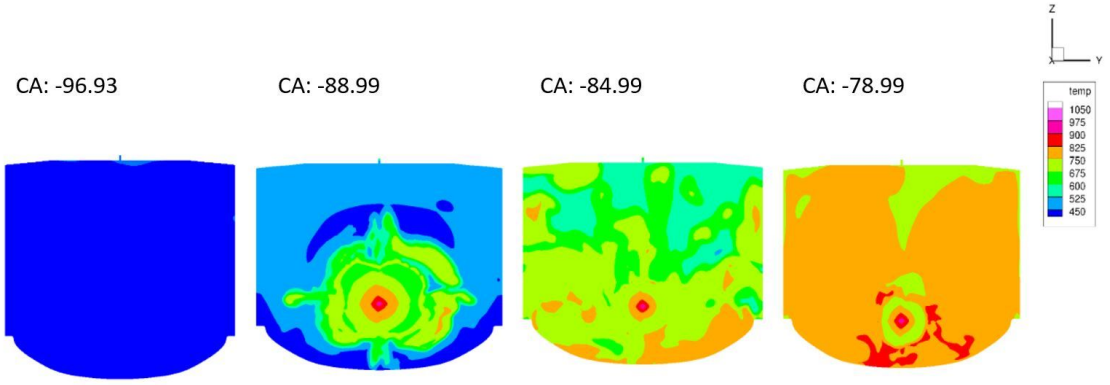

Figure 4.5: Slice visualization of droplet pre-ignition.

Figure 4.4 shows pressure trace results from the two simulations, with oil injection and spark timing specified on the plot. In comparison to the base GDI engine case, the presence of lubricant oil droplet prior to spark timing resulted in a pre-ignition event, and higher peak pressure was observed for this case. Additional visualization can be seen in Figure 4.5, where slices of the combustion chamber's temperature profile at different crank angle degrees are shown. When engine oil droplet was introduced at -90 CAD, the surrounding area of said droplet started to vaporize and form a combustible mixture with presence of surrounding gasoline from prior direct injection. Then, a pre-ignition even occurred, and flame propagation was then observed as this combustible mixture auto-ignited, consuming fuel from direct-injection ahead of spark ignition.

Chapter 5: Conclusions

In summary, a chemical kinetics model was developed specifically for computational studies of LSPI in GDI engines. Sub-models of PRFs and $C_{16}H_{34}$ were included as surrogates for gasoline and lubricant base oil, respectively. An additive package was also incorporated in the model, currently including chemical reactions of sodium and potassium-containing species, to investigate the included compounds' effect on super-knock frequency. Results from preliminary ignition-delay studies showed trends in alignment with reported experimental data from the literature, with higher concentration of sodium additives yielding faster ignition delay times of the fuel/oil mixture. An additional study was carried out using the developed kinetic model in the CONVERGE CFD solver, and found that adding sodium triggers pre-ignition events at low-speed, high-load conditions, leading to higher peak pressure and flame propagation consuming fuel from direct injection prior to spark ignition. These results indicate a promising outlook for this area of research.

Further development is needed for this model, including using a more-detailed chemical kinetic model for gasoline to account for the effects of fuel constituents to LSPI (i.e., aromatic content, oxygenated additives, fuel sensitivity).Additionally, chemistry describing other lubricant oil constituents (i.e., Ca, Fe, Mg, Li) is needed to broaden the size of the current additive package, enabling a parametric approach to determine the most effective lubricant oil formulation to combat LSPI events. More effort is also needed towards utilizing a more elaborate surrogate model for gasoline, as this component of the model also plays an important part in the occurrence of super-knock [10, 32, 66, 93]. Model reduction methods can be used to reduce larger, more detailed gasoline surrogate models in the literature to practical sizes for use in 3D CFD simulations, while retaining relevant components of interest [94, 95]. By including additional components in the surrogate model of gasoline (i.e. toluene, ethanol), the modeling effort from this work can then use a better representation of gasoline. This will allow for more capability in the model, in which the influence of gasoline characteristics (i.e. various aromatics content, anti-knock index) on super-knock occurrence can also be investigated. Engine simulations via 3D CFD will then be implemented, incorporating this reduced chemical

mechanism, to investigate low-speed pre-ignition phenomenon.

Furthermore, sensitivity analysis of the model is needed to determine the anti-super knock quality of components currently included in this work. While the reduction in ignition delay time from having additional sodium-containing compound in the formulation of lubricant oil shown in this work correlates well with reported experimental data, it is unclear which reaction pathways dominate the process and contribute to such results. From the work of Zhang et al., it has been shown that the OH radical contributes as the most important intermediate species in the ignition process and that the anti-knock ability of additives in their study mainly originates from the ability to quench OH radicals or precursors effectively [46]. In the area of super-knock research, however, this presents a promising outlook for further research and development. In doing so, we can better-understand the underlying LSPI physics, and provide further assistance to the development of next-generation gasoline, lubricant oil, and engine technology.

Bibliography

[1] AN Kleit, "Impacts of long-range increases in the fuel economy (cafe) standard", Economic Inquiry **42**, 279–294 (2004) 10.1093/ei/cbh060.

[2] M Amann, D Mehta, and T Alger, "Engine Operating Condition and Gasoline Fuel Composition Effects on Low-Speed Pre-Ignition in High-Performance Spark Ignited Gasoline Engines", SAE International Journal of Engines **4**, 2011–01 (2011) 10.4271/2011-01-0342.

[3] O Welling, J Moss, J Williams, and N Collings, "Measuring the Impact of Engine Oils and Fuels on Low-Speed Pre-Ignition in Downsized Engines", SAE International Journal of Fuels and Lubricants **7**, 2014–01 (2014) 10.4271/2014-01-1219.

[4] M Amann, T Alger, and D Mehta, "The Effect of EGR on Low-Speed Pre-Ignition in Boosted SI Engines", SAE International Journal of Engines **4**, 235–245 (2011) 10.4271/2011-01-0339.

[5] E Chapman, RS Davis, W Studzinski, and P Geng, "Fuel Octane and Volatility Effects on the Stochastic Pre-Ignition Behavior of a 2.0L Gasoline Turbocharged DI Engine", SAE International Journal of Fuels and Lubricants **7**, 379–389 (2014) 10.4271/2014-01-1226.

[6] J Willand, M Daniel, E Montefrancesco, B Geringer, P Hofmann, and M Kieberger, "Limits on downsizing in spark ignition engines due to pre-ignition", MTZ worldwide **70**, 56–61 (2009) 10.1007/BF03226955.

[7] GT Kalghatgi and D Bradley, "Pre-ignition and 'super-knock' in turbo-charged spark-ignition engines", International Journal of Engine Research **13**, 399–414 (2012) 10.1177/1468087411431890.

[8] D Bradley and GT Kalghatgi, "Influence of autoignition delay time characteristics of different fuels on pressure waves and knock in reciprocating engines", Combustion and Flame **156**, 2307–2318 (2009) 10.1016/j.combustflame.2009.08.003.

[9] G Bansal and HG Im, "Autoignition and front propagation in low temperature combustion engine environments", Combustion and Flame **158**, 2105–2112 (2011) 10.1016/j.combustflame.2011.03.019.

[10] M Mayer, P Hofmann, B Geringer, J Williams, and J Moss, "Influence of Different Fuel Properties and Gasoline - Ethanol Blends on Low-Speed Pre-Ignition in Turbocharged Direct Injection Spark Ignition Engines", SAE International Journal of Engines **9**, 841–848 (2016) 10.4271/2016-01-0719.

[11] Z Wang, H Liu, and RD Reitz, "Knocking combustion in spark-ignition engines", Progress in Energy and Combustion Science **61**, 78–112 (2017) 10.1016/j.pecs.2017.03.004.

[12] A Cairns, N Fraser, and H Blaxill, "Pre Versus Post Compressor Supply of Cooled EGR for Full Load Fuel Economy in Turbocharged Gasoline Engines", SAE Technical Paper Series **1**, 776–790 (2010) 10.4271/2008-01-0425.

[13] H Nose, T Inoue, S Katagiri, A Sakai, T Kawasaki, and M Okamura, "Fuel Enrichment Control System by Catalyst Temperature Estimation to Enable Frequent Stoichiometric Operation at High Engine Speed/Load Condition", SAE Technical Paper Series **1** (2013) 10.4271/2013-01-0341.

[14] Z Wang, H Liu, T Song, Y Qi, X He, S Shuai, and J Wang, "Relationship between super-knock and pre-ignition", International Journal of Engine Research **16**, 166–180 (2015) 10.1177/1468087414530388.

[15] C Dahnz, KM Han, U Spicher, M Magar, R Schiessl, and U Maas, *Investigations on Pre-Ignition in Highly Supercharged SI Engines*, 2010, 10.4271/2010-01-0355.

[16] Y Okada, S Miyashita, Y Izumi, and Y Hayakawa, "Study of Low-Speed Pre-Ignition in Boosted Spark Ignition Engine", SAE International Journal of Engines **7**, 584–594 (2014) 10.4271/2014-01-1218.

[17] K Takeuchi, K Fujimoto, S Hirano, and M Yamashita, "Investigation of Engine Oil Effect on Abnormal Combustion in Turbocharged Direct Injection - Spark Ignition Engines", SAE International Journal of Fuels and Lubricants **5**, 2012–01 (2012) 10.4271/2012-01-1615.

[18] O Welling, N Collings, J Williams, and J Moss, "Impact of Lubricant Composition on Low-speed", SAE Technical Paper, 2014–01 (2014) 10.4271/2014-01-1213.Copyright.

[19] M Ohtomo, H Miyagawa, M Koike, N Yokoo, and K Nakata, "Pre-Ignition of Gasoline-Air Mixture Triggered by a Lubricant Oil Droplet", SAE International Journal of Fuels and Lubricants **7**, 673–682 (2014) 10.4271/2014-01-2627.

[20] Y Qi, Y Xu, Z Wang, and J Wang, "The Effect of Oil Intrusion on Super Knock in Gasoline Engine", SAE Technical Paper Series **1** (2014) 10.4271/2014-01-1224.

[21] T Kuboyama, Y Moriyoshi, and K Morikawa, "Visualization and Analysis of LSPI Mechanism Caused by Oil Droplet, Particle and Deposit in Highly Boosted SI Combustion in Low Speed Range", SAE International Journal of Engines **8**, 529–537 (2015) 10.4271/2015-01-0761.

[22] Y Shi, *Computational optimization of internal combustion engines*, London ; New York, 2011.

[23] A Zahdeh, P Rothenberger, W Nguyen, M Anbarasu, S Schmuck-Soldan, J Schaefer, and T Goebel, "Fundamental Approach to Investigate Pre-Ignition in Boosted SI Engines", SAE International Journal of Engines **4**, 2011–01 (2011) 10.4271/2011-01-0340.

[24] JB Haywood, *Internal Combustion Engine Fundamentals, 1989*.

[25] M Amann and T Alger, "Lubricant Reactivity Effects on Gasoline Spark Ignition Engine Knock", SAE International Journal of Fuels and Lubricants **5**, 760–771 (2012) 10.4271/2012-01-1140.

[26] D Downs and FB Theobald, "The Effect of Fuel Characteristics and Engine Operating Conditions on Pre-Ignition", Proceedings of the Institution of Mechanical Engineers: Automobile Division **178**, 89–108 (1963) 10.1243/PIME{_}AUTO{_}1963{_}178{_}016{_}02.

[27] JM Zaccardi and D Escudié, "Overview of the main mechanisms triggering low-speed pre-ignition in spark-ignition engines", International Journal of Engine Research **16**, 152–165 (2015) 10.1177/1468087414530965.

[28] T Inoue, Y Inoue, and M Ishikawa, "Abnormal Combustion in a Highly Boosted SI Engine - The Occurrence of Super Knock", SAE Technical Paper Series **1** (2012) 10.4271/2012-01-1141.

[29] T Lauer, M Heiss, N Bobicic, W Holly, and S Pritze, "A comprehensive simulation approach to irregular combustion", SAE Technical Papers **1** (2014) 10.4271/2014-01-1214.

[30] *Chemistry and technology of lubricants* (Blackie ; VCH, Glasgow : New York, 1992).

[31] G Kalghatgi, *Fuel/Engine Interactions* (SAE International, Oct. 2013).

[32] M Amann, T Alger, B Westmoreland, and A Rothmaier, "The Effects of Piston Crevices and Injection Strategy on Low-Speed Pre-Ignition in Boosted SI Engines", SAE International Journal of Engines **5**, 1216–1228 (2012) 10.4271/2012-01-1148.

[33] S Hirano, M Yamashita, K Fujimoto, and K Kato, "Investigation of Engine Oil Effect on Abnormal Combustion in Turbocharged Direct Injection - Spark Ignition Engines (Part 2)", in Sae international journal of fuels and lubricants, Vol. 5, 3 (Oct. 2013), pp. 2012–01, 10.4271/2013-01-2569.

[34] K Fujimoto, M Yamashita, S Hirano, K Kato, I Watanabe, and K Ito, "Engine Oil Development for Preventing Pre-Ignition in Turbocharged Gasoline Engine", SAE International Journal of Fuels and Lubricants **7**, 2014–01 (2014) 10.4271/2014-01-2785.

[35] A Ritchie, D Boese, and AW Young, "Controlling Low-Speed Pre-Ignition in Modern Automotive Equipment Part 3: Identification of Key Additive Component Types and Other Lubricant Composition Effects on Low-Speed Pre-Ignition", SAE International Journal of Engines **9** (2016) 10.4271/2016-01-0717.

[36] KA Fletcher, L Dingwell, K Yang, WY Lam, and JP Styer, "Engine Oil Additive Impacts on Low Speed Pre-Ignition", SAE International Journal of Fuels and Lubricants **9**, 612–620 (2016) 10.4271/2016-01-2277.

[37] IG Elliott and WV Dam, *Lubricanting Oil Compositions and Method for Preventing or Reducing Low Speed Pre-Ignition in Direct Injected Spark-Ignited Engines*, 2018.

[38] J Styer and G Guinther, "Fuel Economy Beyond ILSAC GF-5: Correlation of Modern Engine Oil Tests to Real World Performance", SAE International Journal of Fuels and Lubricants **5**, 1025–1033 (2012) 10.4271/2012-01-1618.

[39] F Mounce, "Development of a Standardized Test to Evaluate the Effect of Gasoline Engine Oil on the Occurrence of Low Speed Pre-Ignition - The Sequence IX Test", SAE Technical Paper Series **1**, 1–9 (2018) 10.4271/2018-01-1808.

[40] N Peters, B Kerschgens, and G Paczko, "Super-knock prediction using a refined theory of turbulence", SAE International Journal of Engines **6**, 953–967 (2013) 10.4271/2013-01-1109.

[41] G Kalghatgi, "Knock onset, knock intensity, superknock and preignition in spark ignition engines", International Journal of Engine Research **19**, 7–20 (2018) 10.1177/1468087417736430.

[42] Y Moriyoshi, T Yamada, D Tsunoda, M Xie, T Kuboyama, and K Morikawa, "Numerical Simulation to Understand the Cause and Sequence of LSPI Phenomena and Suggestion of CaO Mechanism in Highly Boosted SI Combustion in Low Speed Range", SAE Technical Papers **2015-April** (2015) 10.4271/2015-01-0755.

[43] T Tsurushima, "A new skeletal PRF kinetic model for HCCI combustion", Proceedings of the Combustion Institute **32 II**, 2835–2841 (2009) 10.1016/j.proci.2008.06.018.

[44] MJ Mubarak Ali, F Hernandez Perez, S Vedharaj, R Vallinayagam, R Dibble, and H Im, "Effect of Timing and Location of Hotspot on Super Knock during Pre-ignition", SAE Technical Papers **2017-March** (2017) 10.4271/2017-01-0686.

[45] MJ Mubarak Ali, F Hernandez Perez, A Sow, and H Im, "A Computational Study of Abnormal Combustion Characteristics in Spark Ignition Engines", SAE Technical Papers **2018-April**, 1–11 (2018) 10.4271/2018-01-0179.

[46] P Zhang, NW Yee, SV Filip, CE Hetrick, B Yang, and WH Green, "Modeling study of the anti-knock tendency of substituted phenols as additives: an application of the reaction mechanism generator (RMG)", Physical Chemistry Chemical Physics **20**, 10637–10649 (2018) 10.1039/C7CP07058F.

[47] E Distaso, R Amirante, G Calò, PD Palma, P Tamburrano, and R Reitz, "Investigation of Lubricant Oil influence on Ignition of Gasoline-like Fuels by a Detailed Reaction Mechanism", Energy Procedia **148**, 663–670 (2018) 10.1016/j.egypro.2018.08.155.

[48] H Wang, M Yao, and RD Reitz, "Development of a reduced primary reference fuel mechanism for internal combustion engine combustion simulations", Energy and Fuels **27**, 7843–7853 (2013) 10.1021/ef401992e.

[49] SM Sarathy, CK Westbrook, M Mehl, WJ Pitz, C Togbe, P Dagaut, H Wang, MA Oehlschlaeger, U Niemann, K Seshadri, PS Veloo, C Ji, FN Egolfopoulos, and T Lu, "Comprehensive chemical kinetic modeling of the oxidation of 2-methylalkanes from C7 to C20", Combustion and Flame **158**, 2338–2357 (2011) 10.1016/j.combustflame.2011.05.007.

[50] S Sarathy, A Farooq, and GT Kalghatgi, "Recent progress in gasoline surrogate fuels", Progress in Energy and Combustion Science **65**, 67–108 (2018) 10.1016/j.pecs.2017.09.004.

[51] YD Liu, M Jia, MZ Xie, and B Pang, "Enhancement on a skeletal kinetic model for primary reference fuel oxidation by using a semidecoupling methodology", Energy and Fuels **26**, 7069–7083 (2012) 10.1021/ef301242b.

[52] American Petroleum Institute, "Engine Oil Licensing and Certification System", **1**, E1–E29 (2012).

[53] CK Westbrook, WJ Pitz, O Herbinet, HJ Curran, and EJ Silke, "A comprehensive detailed chemical kinetic reaction mechanism for combustion of n-alkane hydrocarbons from n-octane to n-hexadecane", Combustion and Flame **156**, 181–199 (2009) 10.1016/j.combustflame.2008.07.014.

[54] A Ristori, P Dagaut, and M Cathonnet, "The oxidation of n-Hexadecane: experimental and detailed kinetic modeling", Combustion and Flame **125**, 1128–1137 (2001) 10.1016/S0010-2180(01)00232-2.

[55] C Chevalier, W Pitz, J Warnatz, C Westbrook, and H Melenk, "Hydrocarbon ignition: Automatic generation of reaction mechanisms and applications to modeling of engine knock", Symposium (International) on Combustion **24**, 93–101 (1992) 10.1016/S0082-0784(06)80016-0.

[56] O Herbinet, WJ Pitz, and CK Westbrook, "Detailed chemical kinetic oxidation mechanism for a biodiesel surrogate", Combustion and Flame **154**, 507–528 (2008) 10.1016/j.combustflame.2008.03.003.

[57] E Ranzi, A Frassoldati, S Granata, and T Faravelli, "Wide-Range Kinetic Modeling Study of the Pyrolysis, Partial Oxidation, and Combustion of Heavy n -Alkanes", Industrial & Engineering Chemistry Research **44**, 5170–5183 (2005) 10.1021/ie049318g.

[58] R Fournet, F Battin-Leclerc, PA Glaude, B Judenherc, V Warth, GM Côme, G Scacchi, A Ristori, G Pengloan, P Dagaut, and M Cathonnet, "The gas-phase oxidation of n -hexadecane", International Journal of Chemical Kinetics **33**, 574–586 (2001) 10.1002/kin.1053.

[59] OA Kuti, SY Yang, N Hourani, N Naser, WL Roberts, SH Chung, and SM Sarathy, "A fundamental investigation into the relationship between lubricant composition and fuel ignition quality", Fuel **160**, 605–613 (2015) 10.1016/j.fuel.2015.08.026.

[60] M Assad, V Leschevich, P O.G., K Sevrouk, V Tangirala, and J N. D., "Autoignitions of N-hexadecane and heptamethylnonane at high temperatures", Nonequilibrium phenomena. Plasma, combustion, atmosphere, 210–220 (2009).

[61] H Kawanabe and T Ishiyama, "A Study on a Reduced Kinetic Model for n-Cetane and Heptamethylnonane Based on a PRF Reduced Kinetic Model", SAE Technical Paper Series **1** (2012) 10.4271/2012-01-1576.

[62] Y Chang, M Jia, Y Liu, Y Li, M Xie, and H Yin, "Application of a decoupling methodology for development of skeletal oxidation mechanisms for heavy n -alkanes from n -octane to n -hexadecane", Energy and Fuels **27**, 3467–3479 (2013) 10.1021/ef400460d.

[63] HPS Shen and MA Oehlschlaeger, "The autoignition of C8H10 aromatics at moderate temperatures and elevated pressures", Combustion and Flame **156**, 1053–1062 (2009) 10.1016/j.combustflame.2008.11.015.

[64] DR Haylett, DF Davidson, and RK Hanson, "Ignition delay times of low-vapor-pressure fuels measured using an aerosol shock tube", Combustion and Flame **159**, 552–561 (2012) 10.1016/j.combustflame.2011.08.021.

[65] SR Turns, *An introduction to combustion : concepts and applications*, Boston, 2000.

[66] M Kassai, K Torii, T Shiraishi, T Noda, TK Goh, K Wilbrand, S Wakefield, A Healy, D Doyle, R Cracknell, and M Shibuya, "Research on the Effect of Lubricant Oil and Fuel Properties on LSPI Occurrence in Boosted S. I. Engines", SAE Technical Paper Series **1** (2016) 10.4271/2016-01-2292.

[67] VV Lissianski, VM Zamansky, and PM Maly, "Effect of metal-containing additives on NOx reduction in combustion and reburning", Combustion and Flame **125**, 1118–1127 (2001) 10.1016/S0010-2180(01)00231-0.

[68] RA Perry and JA Miller, "An exploratory investigation of the use of alkali metals in nitrous oxide control", International Journal of Chemical Kinetics **28**, 217–234 (1996) 10.1002/(SICI)1097-4601(1996)28:3<217::AID-KIN7>3.0.CO;2-Y.

[69] VM Zamansky, VV Lissianski, PM Maly, L Ho, D Rusli, and WC Gardiner, "Reactions of sodium species in the promoted SNCR process", Combustion and Flame **117**, 821–831 (1999) 10.1016/S0010-2180(98)00127-8.

[70] VM Zamansky, PM Maly, L Ho, VV Lissianski, D Rusli, and WC Gardiner, "Promotion of selective non-catalytic reduction of no by sodium carbonate", Symposium (International) on Combustion **27**, 1443–1449 (1998) 10.1016/S0082-0784(98)80551-1.

[71] P Glarborg and P Marshall, "Mechanism and modeling of the formation of gaseous alkali sulfates", Combustion and Flame **141**, 22–39 (2005) 10.1016/j.combustflame.2004.08.014.

[72] L Hindiyarti, F Frandsen, H Livbjerg, P Glarborg, and P Marshall, "An exploratory study of alkali sulfate aerosol formation during biomass combustion", Fuel **87**, 1591–1600 (2008) 10.1016/j.fuel.2007.09.001.

[73] K Tran, KE Niemeyer, and CL Hagen, *Reduced chemical kinetics model for PRFs, n-hexadecane, and sodium/potassium additives*, Sept. 2019, 10.5281/zenodo.3459928.

[74] HK(K Versteeg, *An introduction to computational fluid dynamics : the finite volume method*, Harlow, England ; New York, 2007.

[75] Convergent Science, "CONVERGE Manual v2.4", 1008 (2017).

[76] FM White, *Fluid mechanics*, New York, 2008.

[77] Z Han and RD Reitz, "Turbulence Modeling of Internal Combustion Engines Using RNG κ-ϵ Models", Combustion Science and Technology **106**, 267–295 (1995) 10.1080/00102209508907782.

[78] PR Spalart, S Deck, ML Shur, KD Squires, MK Strelets, and A Travin, "A New Version of Detached-eddy Simulation, Resistant to Ambiguous Grid Densities", Theoretical and Computational Fluid Dynamics **20**, 181–195 (2006) 10.1007/s00162-006-0015-0.

[79] A Yoshizawa and K Horiuti, "A Statistically-Derived Subgrid-Scale Kinetic Energy Model for the Large-Eddy Simulation of Turbulent Flows", Journal of the Physical Society of Japan **54**, 2834–2839 (1985) 10.1143/JPSJ.54.2834.

[80] M Halstead, L Kirsch, and C Quinn, "The autoignition of hydrocarbon fuels at high temperatures and pressures—Fitting of a mathematical model", Combustion and Flame **30**, 45–60 (1977) 10.1016/0010-2180(77)90050-5.

[81] PK Senecal, E Pomraning, KJ Richards, TE Briggs, CY Choi, RM McDavid, and MA Patterson, "Multi-dimensional modeling of direct-injection diesel spray liquid length and flame lift-off length using cfd and parallel detailed chemistry", SAE Technical Papers (2003) 10.4271/2003-01-1043.

[82] RD Reltz and Tw Kuo, "Modeling of HC Emissions Due to Crevice Flows in Premixed-Charge Engines", in (Sept. 1989), 10.4271/892085.

[83] PK Senecal, KJ Richards, E Pomraning, T Yang, MZ Dai, RM McDavid, MA Patterson, S Hou, and T Shethaji, "A New Parallel Cut-Cell Cartesian CFD Code for Rapid Grid Generation Applied to In-Cylinder Diesel Engine Simulations", in (Apr. 2007), 10.4271/2007-01-0159.

[84] P Senecal, D Schmidt, I Nouar, C Rutland, R Reitz, and M Corradini, "Modeling high-speed viscous liquid sheet atomization", International Journal of Multiphase Flow **25**, 1073–1097 (1999) 10.1016/S0301-9322(99)00057-9.

[85] PJ O'Rourke and AA Amsden, "The Tab Method for Numerical Calculation of Spray Droplet Breakup", in (Nov. 1987), 10.4271/872089.

[86] P Vesilind, "The Rosin-Rammler particle size distribution", Resource Recovery and Conservation **5**, 275–277 (1980) 10.1016/0304-3967(80)90007-4.

[87] PJ O'Rourke, "Collective drop effects on vaporizing liquid sprays",

[88] DP Schmidt and C Rutland, "A New Droplet Collision Algorithm", Journal of Computational Physics **164**, 62–80 (2000) 10.1006/jcph.2000.6568.

[89] SL Post and J Abraham, "Modeling the outcome of drop–drop collisions in Diesel sprays", International Journal of Multiphase Flow **28**, 997–1019 (2002) 10.1016/S0301-9322(02)00007-1.

[90] AA Amsden, "KIVA-3V: A Block-Structured KIVA Program for Engines with Vertical or Canted Valves", LA Report (1997) 10.1016/0375-6505(82)90028-1.

[91] CONVERGE, "CONVERGE Studio Manual v2.4", (2018).

[92] M Kassai, H Hashimoto, T Shiraishi, A Teraji, and T Noda, "Mechanism Analysis on LSPI Occurrence in Boosted S. I. Engines", SAE Technical Paper Series **1** (2015) 10.4271/2015-01-1867.

[93] P Haenel, H Kleeberg, R de Bruijn, and D Tomazic, "Influence of Ethanol Blends on Low Speed Pre-Ignition in Turbocharged, Direct-Injection Gasoline Engines", SAE International Journal of Fuels and Lubricants **10**, 95–105 (2017) 10.4271/2017-01-0687.

[94] KE Niemeyer and Cj Sung, "On the importance of graph search algorithms for DRGEP-based mechanism reduction methods", **158**, 1439–1443 (2011) 10.1016/j.combustflame.2010.12.010.

[95] KE Niemeyer, CJ Sung, and MP Raju, "Skeletal mechanism generation for surrogate fuels using directed relation graph with error propagation and sensitivity analysis", Combustion and Flame (2010) 10.1016/j.combustflame.2009.12.022.

APPENDICES

Appendix A: Chemical kinetics model for PRFs

Table 1: Chemical kinetics model for PRFs from Liu at al. [51].

no.	reactions (k = AT**b exp(-E/RT))	A	b	E
1	C7H16+O2=C7H15+HO2	1.00E+16	0	46000
	Rev:	1.00E+12	0	0
2	C7H16+OH=>C7H15+H2O	5.00E+13	0	3000
3	C7H16+HO2=>C7H15+H2O2	1.00E+13	0	16950
4	C7H15+O2=C7H15O2	3.00E+12	0	0
	Rev:	2.51E+13	0	27400
5	C7H15O2=C7H14OOH	1.51E+11	0	19000
	Rev:	1.00E+11	0	11000
6	C7H14OOH+O2=O2C7H14OOH	6.16E+10	0	0
	Rev:	2.51E+13	0	27400
7	O2C7H14OOH=>C7KET+OH	8.91E+10	0	17000
8	C7H15+O2=C7H14+HO2	3.16E+11	0	6000
	Rev:	3.16E+11	0	19500
9	C7KET=>C5H11CO+CH2O+OH	3.98E+15	0	43000
10	C5H11CO+O2=>C3H7+C2H3+CO+HO2	3.16E+13	0	10000
11	C7H14+O2=>C3H6+C2H5+CH2O+HCO	3.16E+13	0	10000
12	C7H15=>C3H6+C2H5+C2H4	6.50E+12	0	28810
13	C8H18+O2=C8H17+HO2	6.00E+15	0	46000
	Rev:	1.00E+12	0	0
14	C8H18+OH=>C8H17+H2O	2.00E+13	0	3000
15	C8H18+HO2=>C8H17+H2O2	1.00E+13	0	16950
16	C8H17+O2=C8H17O2	1.00E+12	0	0
	Rev:	2.51E+13	0	27400
17	C8H17O2=C8H16OOH	1.51E+11	0	21800
	Rev:	1.00E+11	0	11000
18	C8H16OOH+O2=O2C8H16OOH	1.16E+11	0	0
	Rev:	2.51E+13	0	27400
19	O2C8H16OOH=>C8KET+OH	8.91E+10	0	17000

Table 1 continued from previous page

20	C8H17+O2=C8H16+HO2	3.16E+11	0	6000
	Rev:	3.16E+11	0	19500
21	C8KET=>C6H13CO+CH2O+OH	3.98E+15	0	43000
22	C6H13CO+O2=>C3H7+C3H5+CO+HO2	3.16E+13	0	10000
23	C8H16+O2=>C3H7+C3H6+CH2O+HCO	3.16E+13	0	10000
24	C8H17=>C3H7+C3H6+C2H4	1.12E+17	-1.3	29700
25	C3H7=C2H4+CH3	9.60E+13	0	30950
26	C3H7=C3H6+H	1.25E+14	0	36900
27	C3H6=C2H3+CH3	3.15E+15	0	85500
28	C3H6+CH3=C3H5+CH4	9.00E+12	0	8480
29	C3H5+O2=C3H4+HO2	6.00E+11	0	10000
30	C3H4+OH=C2H3+CH2O	1.00E+12	0	0
31	C3H4+OH=C2H4+HCO	1.00E+12	0	0
32	C2H5+O2=C2H4+HO2	2.00E+10	0	-2200.0
33	C2H4+OH=CH2O+CH3	6.00E+13	0	960
34	C2H4+OH=C2H3+H2O	8.02E+13	0	5955
35	C2H3+O2=CH2O+HCO	4.00E+12	0	-250.0
36	C2H3+HCO=C2H4+CO	6.03E+13	0	0
37	H+O2=O+OH	3.55E+15	-0.4	16599
38	O+H2=H+OH	5.08E+04	2.7	6290
39	H2+OH=H2O+H	2.16E+08	1.5	3430
40	O+H2O=OH+OH	2.97E+06	2	13400
41	H2+M=H+H+M	4.58E+19	-1.4	104380
	H2 enhanced by 2.500			
	H2O enhanced by 1.200e1			
	CO enhanced by 1.900			
	CO2 enhanced by 3.800			
42	O+O+M=O2+M	6.16E+15	-0.5	0
	H2 enhanced by 2.500			
	H2O enhanced by 1.200e1			
	CO enhanced by 1.900			

Table 1 continued from previous page

	CO2 enhanced by 3.800			
43	O+H+M=OH+M	4.71E+18	-1.0	0
	H2 enhanced by 2.500			
	H2O enhanced by 1.200e1			
	CO enhanced by 1.900			
	CO2 enhanced by 3.800			
44	H+OH+M=H2O+M	3.80E+22	-2.0	0
	H2 enhanced by 2.500			
	H2O enhanced by 1.200e1			
	CO enhanced by 1.900			
	CO2 enhanced by 3.800			
45	H+O2(+M)=HO2(+M)	1.48E+12	0.6	0
	low pressure limit:	6.37E+20	-0.17200e1	5.25E+02
	TROE centering:	0.8	0.10000e-29	1.00E+30
	H2 enhanced by 2.000			
	H2O enhanced by 1.100e1			
	O2 enhanced by 7.800e-1			
	CO enhanced by 1.900			
	CO2 enhanced by 3.800			
46	HO2+H=H2+O2	1.66E+13	0	823
47	HO2+H=OH+OH	7.08E+13	0	295
48	HO2+O=O2+OH	3.25E+13	0	0
49	HO2+OH=H2O+O2	2.89E+13	0	-497.0
50	HO2+HO2=H2O2+O2	4.20E+14	0	11982
	Duplicate			
51	HO2+HO2=H2O2+O2	1.30E+11	0	-1629.3
	Duplicate			
52	H2O2(+M)=OH+OH(+M)	2.95E+14	0	48430
	low pressure limit:	1.20E+17	0	4.55E+04
	TROE centering:	0.5	0.10000e-29	1.00E+30
	H2 enhanced by 2.500			

Table 1 continued from previous page

	H2O enhanced by 1.200e1			
	CO enhanced by 1.900			
	CO2 enhanced by 3.800			
53	H2O2+H=H2O+OH	2.41E+13	0	3970
54	H2O2+H=HO2+H2	4.82E+13	0	7950
55	H2O2+O=OH+HO2	9.55E+06	2	3970
56	H2O2+OH=HO2+H2O	1.00E+12	0	0
	Duplicate			
57	H2O2+OH=HO2+H2O	5.80E+14	0	9557
	Duplicate			
58	CO+O(+M)=CO2(+M)	1.80E+10	0	2384
	low pressure limit:	1.55E+24	-0.27900e1	4.19E+03
	H2 enhanced by 2.500			
	H2O enhanced by 1.200e1			
	CO enhanced by 1.900			
	CO2 enhanced by 3.800			
59	CO+O2=CO2+O	2.53E+12	0	47700
60	CO+HO2=CO2+OH	3.01E+13	0	23000
61	CO+OH=CO2+H	2.23E+05	1.9	-1158.7
62	HCO+M=H+CO+M	4.75E+11	0.7	14874
	H2 enhanced by 2.500			
	H2O enhanced by 6.000			
	CO enhanced by 1.900			
	CO2 enhanced by 3.800			
63	HCO+O2=CO+HO2	7.58E+12	0	410
64	HCO+H=CO+H2	7.23E+13	0	0
65	HCO+O=CO+OH	3.02E+13	0	0
66	HCO+OH=CO+H2O	3.02E+13	0	0
67	HCO+O=CO2+H	3.00E+13	0	0
68	HCO+HO2=CO2+OH+H	3.00E+13	0	0
69	HCO+CH3=CO+CH4	1.20E+14	0	0

Table 1 continued from previous page

70	HCO+HCO=H2+CO+CO	3.00E+12	0	0	
71	HCO+HCO=CH2O+CO	3.00E+13	0	0	
72	CH2O+M=HCO+H+M	3.30E+39	-6.3	99900	
	H2 enhanced by 2.500				
	H2O enhanced by 1.200e1				
	CO enhanced by 1.900				
	CO2 enhanced by 3.800				
73	CH2O+M=CO+H2+M	3.10E+45	-8.0	97510	
	H2 enhanced by 2.500				
	H2O enhanced by 1.200e1				
	CO enhanced by 1.900				
	CO2 enhanced by 3.800				
74	CH2O+H=HCO+H2	5.74E+07	1.9	2748.6	
75	CH2O+O=HCO+OH	1.81E+13	0	3080	
76	CH2O+OH=HCO+H2O	3.43E+09	1.2	-447.0	
77	CH2O+O2=HCO+HO2	1.23E+06	3	52000	
78	CH2O+HO2=HCO+H2O2	4.11E+04	2.5	10210	
79	CH2O+CH3=HCO+CH4	3.64e-6	5.4	998	
80	CH3+O=CH2O+H	8.43E+13	0	0	
81	CH3+O2=CH3O+O	1.99E+18	-1.6	29230	
82	CH3+O2=CH2O+OH	3.74E+11	0	14640	
83	CH3+HO2=CH3O+OH	2.41E+10	0.8	-2325.0	
84	CH3+H(+M)=CH4(+M)	1.27E+16	-0.6	383	
	low pressure limit:	0.24770e34	-0.47600e1	2.44E+03	
	TROE centering:	0.783	7.40E+01	2.94E+03	6.96E+03
	H2 enhanced by 2.000				
	H2O enhanced by 6.000				
	CH4 enhanced by 2.000				
	CO enhanced by 1.500				
	CO2 enhanced by 2.000				
85	CH4+H=CH3+H2	5.47E+07	2	11210	

Table 1 continued from previous page

86	CH4+O=CH3+OH	3.15E+12	0.5	10290
87	CH4+OH=CH3+H2O	5.72E+06	2	2639
88	CH3+HO2=CH4+O2	3.16E+12	0	0
89	CH4+HO2=CH3+H2O2	1.81E+11	0	18580
90	CH2OH+M=CH2O+H+M	1.00E+14	0	25100
91	CH2OH+H=CH2O+H2	6.00E+12	0	0
92	CH2OH+H=CH3+OH	9.64E+13	0	0
93	CH2OH+O=CH2O+OH	4.20E+13	0	0
94	CH2OH+OH=CH2O+H2O	2.40E+13	0	0
95	CH2OH+O2=CH2O+HO2	2.41E+14	0	5017
	Duplicate			
96	CH2OH+O2=CH2O+HO2	1.51E+15	-1.0	0
	Duplicate			
97	CH2OH+HO2=CH2O+H2O2	1.20E+13	0	0
98	CH2OH+HCO=CH3OH+CO	1.00E+13	0	0
99	CH2OH+HCO=CH2O+CH2O	1.50E+13	0	0
100	2CH2OH=CH3OH+CH2O	3.00E+12	0	0
101	CH2OH+CH3O=CH3OH+CH2O	2.40E+13	0	0
102	CH3O+M=CH2O+H+M	8.30E+17	-1.2	15500
103	CH3O+H=CH3+OH	3.20E+13	0	0
104	CH3O+O=CH2O+OH	6.00E+12	0	0
105	CH3O+OH=CH2O+H2O	1.80E+13	0	0
106	CH3O+O2=CH2O+HO2	9.03E+13	0	11980
	Duplicate			
107	CH3O+O2=CH2O+HO2	2.20E+10	0	1748
	Duplicate			
108	CH3O+HO2=CH2O+H2O2	3.00E+11	0	0
109	CH3O+CO=CH3+CO2	1.60E+13	0	11800
110	CH3O+HCO=CH3OH+CO	9.00E+13	0	0
111	2CH3O=CH3OH+CH2O	6.00E+13	0	0
112	OH+CH3(+M)≤>CH3OH(+M)	2.79E+18	-1.4	1330

Table 1 continued from previous page

	low pressure limit:	4.00E+36	-0.59200e1	3.14E+03	
	TROE centering:	0.412	1.95E+02	5.90E+03	6.39E+03
	H2 enhanced by 2.000				
	H2O enhanced by 6.000				
	CH4 enhanced by 2.000				
	CO enhanced by 1.500				
	CO2 enhanced by 2.000				
113	H+CH2OH(+M)≤>CH3OH(+M)	1.06E+12	0.5	86	
	low pressure limit:	4.36E+31	-0.46500e1	5.08E+03	
	TROE centering:	0.6	1.00E+02	9.00E+04	1.00E+04
	H2 enhanced by 2.000				
	H2O enhanced by 6.000				
	CH4 enhanced by 2.000				
	CO enhanced by 1.500				
	CO2 enhanced by 2.000				
114	H+CH3O(+M)≤>CH3OH(+M)	2.43E+12	0.5	50	
	Low pressure limit:	4.66E+41	-0.74400e1	1.41E+04	
	TROE centering:	0.7	1.00E+02	9.00E+04	1.00E+04
	H2 enhanced by 2.000				
	H2O enhanced by 6.000				
	CH4 enhanced by 2.000				
	CO enhanced by 1.500				
	CO2 enhanced by 2.000				
115	CH3OH+H=CH2OH+H2	3.20E+13	0	6095	
116	CH3OH+H=CH3O+H2	8.00E+12	0	6095	
117	CH3OH+O=CH2OH+OH	3.88E+05	2.5	3080	
118	CH3OH+OH=CH3O+H2O	1.00E+06	2.1	496.7	
119	CH3OH+OH=CH2OH+H2O	7.10E+06	1.8	-596.0	
120	CH3OH+O2=CH2OH+HO2	2.05E+13	0	44900	
121	CH3OH+HCO=CH2OH+CH2O	9.64E+03	2.9	13110	
122	CH3OH+HO2=CH2OH+H2O2	3.98E+13	0	19400	

Table 1 continued from previous page

123	CH3OH+CH3=CH2OH+CH4	3.19E+01	3.2	7172
124	CH3O+CH3OH=CH3OH+CH2OH	3.00E+11	0	4060

Appendix B: Chemical kinetics model for potassium

Table 2: Chemical kinetics model for potassium-containing species from Glaborg, Miller, and Hindiyarti et al. [71, 72]

no.	reactions (k = AT**b exp(?E/RT))	A	b	E
1	SO2 + O(+M) = SO3(+M)	3.70E+11	0	850
	Low-pressure limit	2.40E+27	?3.60	2610
	Troe parameters: 0.442 316 7442			
	Third-body efficiencies: N2 = 1.3, H2O = 10, SO2 = 10			
2	SO2 + OH = SO3 + H	4.90E+02	2.69	12000
3	SO2 + OH(+M) = HOSO2(+M)	7.20E+12	0	360
	Low-pressure limit	4.50E+25	3.30	360
	Troe parameters: 0.70 1E30 1E30			
	Third-body efficiencies: N2 = 1.5, H2O = 10, SO2 = 10			
4	SO3 + O = SO2 + O2	1.30E+12	0	3070
5	SO3 + SO = SO2 + SO2	7.60E+03	2.37	1500
6	HOSO2 + O2 = SO3 + HO2	7.80E+11	0	330
7	K + O + M = KO+M	1.50E+21	-1.50	0
8	K + OH + M = KOH+M	5.40E+21	-1.55	0
9	K + HO2 = KOH + O	1.00E+14	0	0
10	K + HO2 = KO + OH	3.00E+13	0	0
11	K + O2(+M) = KO2(+M)	3.60E+14	0	0
	Low-pressure limit	5.40E+21	-1.32	0
12	K + H2O2 = KOH + OH	2.50E+13	0	0
13	K + H2O2 = KO + H2O	1.60E+13	0	0
14	KO + H = K + OH	2.00E+14	0	0
15	KO + O = K + O2	2.20E+14	0	0
16	KO + OH = KOH + O	2.00E+13	0	0
17	KO + HO2 = KOH + O2	5.00E+13	0	0
18	KO + H2 = KOH + H	1.60E+13	0	0
19	KO + H2 = K + H2O	3.10E+12	0	0
20	KO + H2O = KOH + OH	1.30E+14	0	0

Table 2 continued from previous page

21	KO + CO = K + CO2	1.00E+14	0	0
22	KOH + H = K + H2O	5.00E+13	0	0
23	KOH + KOH = (KOH)2	8.00E+13	0	0
24	KO2 + H = K + HO2	2.00E+14	0	0
25	KO2 + H = KO + OH	5.00E+13	0	0
26	KO2 + H = KOH + O	1.00E+14	0	0
27	KO2 + O = KO + O2	1.30E+13	0	0
28	KO2 + OH = KOH + O2	2.00E+13	0	0
29	KO2 + CO = KO + CO2	1.00E+14	0	0
30	K + Cl + M = KCl+M	1.80E+20	-1.00	0
31	K + HCl = KCl + H	9.10E+12	0	594
	Duplicate reaction	1.00E+14	0	1830
32	K + Cl2 = KCl + Cl	4.40E+14	0	0
33	K + ClO = KCl + O	1.00E+14	0	0
34	KO + HCl = KCl + OH	1.70E+14	0	0
35	KOH + HCl = KCl + H2O	1.70E+14	0	0
36	KO2 + Cl = KCl + O2	1.00E+14	0	0
37	KO2 + HCl = KCl + HO2	1.40E+14	0	0
38	KCl + KCl = (KCl)2	8.00E+13	0	0
39	K + SO2(+M) = KSO2(+M)	3.70E+14	0	0
	Low-pressure limit	5.20E+23	-1.50	0
40	K + SO3 (+M) = KSO3(+M)	3.70E+14	0	0
	Low-pressure limit	4.70E+34	-4.90	0
41	K + SO3 = KO + SO2	1.00E+14	0	7840
42	KO + SO2(+M) = KSO3(+M)	3.70E+14	0	0
	Low-pressure limit	5.20E+23	-1.50	0
43	KOH + SO3(+M) = KHSO4(+M)	1.00E+14	0	0
	Low-pressure limit	2.60E+42	-7.6	0
44	KSO2 + O = KO + SO2	1.30E+13	0	0
45	KSO2 + OH = KOH + SO2	2.00E+13	0	0
46	KSO2 + KO2 = K2SO4	1.00E+14	0	0

Table 2 continued from previous page

47	KSO3 + O = KO + SO3	1.30E+13	0	0
48	KSO3 + OH = KOH + SO3	2.00E+13	0	0
49	KSO3 + KO = K2SO4	1.00E+14	0	0
50	KHSO4 + KOH = K2SO4 + H2O	1.00E+14	0	0
51	KHSO4 + KCl = K2SO4 + HCl	1.00E+14	0	0
52	KCl + SO3(+M) = KSO3Cl(+M)	1.00E+14	0	0
	Low-pressure limit	1.90E+41	-7.80	0
53	KSO3Cl + OH = KHSO4 + Cl	1.00E+14	0	0
54	KSO3Cl + H2O = KHSO4 + HCl	1.00E+14	0	0
55	KSO3Cl + KOH = K2SO4 + HCl	1.00E+14	0	0

Appendix C: Python script for ignition delay studies

```
# -*- coding: utf-8 -*-
"""
Created on Tue Apr 2 14:17:05 2019

@author: Khang Tran
"""

from __future__ import division
from __future__ import print_function

import pandas as pd
import numpy as np

import time

import cantera as ct
print('Runnning Cantera version: ' + ct.__version__)
import matplotlib.pyplot as plt


plt.rcParams['axes.labelsize'] = 18
plt.rcParams['xtick.labelsize'] = 12
plt.rcParams['ytick.labelsize'] = 12
plt.rcParams['figure.autolayout'] = True

plt.style.use('ggplot')
plt.style.use('seaborn-pastel')

mechanism = 'C:\\Users\\esl1\\Desktop\\Ignition Delay Study\\PythonIgnitionDelayCode\\OSULSPIMech3.cti'
gas = ct.Solution(mechanism)
# Define the reactor temperature and pressure
#reactorTemperature = 680 #Kelvin
#reactorPressure = 1500000.0 #Pascals

#gas.TP = reactorTemperature, reactorPressure

# Define the fuel, oxidizer and set the stoichiometry
#gas.set_equivalence_ratio(phi=0.8, fuel={'IC8H18':0.99431818181818187,'C16H34':0.0056818181818181823}, oxidizer={'o2':1.0, 'n2
      ':3.76})

# Create a batch reactor object and add it to a reactor network
# In this example, the batch reactor will be the only reactor
# in the network
r = ct.IdealGasReactor(contents=gas, name='Batch Reactor')
reactorNetwork = ct.ReactorNet([r])

# now compile a list of all variables for which we will store data
stateVariableNames = [r.component_name(item) for item in range(r.n_vars)]

# use the above list to create a DataFrame
timeHistory = pd.DataFrame(columns=stateVariableNames)
def ignitionDelay(df, species):
    """
    This function computes the ignition delay from the occurence of the
    peak in species' concentration.
    """
    return df[species].idxmax()
#Tic
# Make a list of all the temperatures we would like to run simulations at
T = [650,700,750,800,850,900,950,1000,1050,1100,1150,1200,1250,1300,1350,1400,1450,1500,1550]
```

```
estimatedIgnitionDelayTimes = np.ones(len(T))

# Make time adjustments for the highest and lowest temperatures. This we do empirically
estimatedIgnitionDelayTimes[:6] = 6*[0.1]
estimatedIgnitionDelayTimes[-2:] = 10
estimatedIgnitionDelayTimes[-1] = 100

# Now create a dataFrame out of these
ignitionDelays = pd.DataFrame(data={'T': T})
ignitionDelays['ignDelay'] = np.nan


for i, temperature in enumerate(T):
    # Setup the gas and reactor
    reactorTemperature = temperature
    reactorPressure = 20.0*ct.one_atm
    gas.TP = reactorTemperature, reactorPressure
    gas.set_equivalence_ratio(phi=1, fuel={'IC8H18':0.25,'C16H34':0.7425,'K':0.0075}, oxidizer={'O2':1.0, 'N2':3.76})
    r = ct.IdealGasReactor(contents=gas, name='Batch Reactor')
    reactorNetwork = ct.ReactorNet([r])

    # Create and empty data frame
    timeHistory = pd.DataFrame(columns=timeHistory.columns)

    t0 = time.time()

    t = 0
    counter = 0
    while t < estimatedIgnitionDelayTimes[i]:
        t = reactorNetwork.step()
        if not counter % 20:
            timeHistory.loc[t] = r.get_state()
        counter += 1

    tau = ignitionDelay(timeHistory, 'OH')
    t1 = time.time()

    print('Computed Ignition Delay: {:.3e} seconds for T={}K. Took {:3.2f}s to compute'.format(tau, temperature, t1-t0))

    ignitionDelays.at[i, 'ignDelay'] = tau



export_csv = ignitionDelays.to_csv (r'C:\\Users\\esl1\\Desktop\\Ignition Delay Study\\PythonIgnitionDelayCode\\IgnitionDelayC8H18+
      C16H34+1%K.csv', index = None, header=True)

fig = plt.figure()
ax = fig.add_subplot(111)
ax.semilogy(1000/ignitionDelays['T'], ignitionDelays['ignDelay'], 'o-')
ax.set_ylabel('Ignition Delay (s)')
ax.set_xlabel(r'$\frac{1000}{T (K)}$', fontsize=18)

# Add a second axis on top to plot the temperature for better readability
ax2 = ax.twiny()
ticks = ax.get_xticks()
ax2.set_xticks(ticks)
ax2.set_xticklabels((1000/ticks).round(1))
ax2.set_xlim(ax.get_xlim())
ax2.set_xlabel(r'Temperature: $T(K)$');
# If you want to save all the data - molefractions, temperature, pressure, etc
# uncomment the next line
# timeHistory.to_csv("time_history.csv")
```

Appendix D: Python scripts for jet-stirred reactor species concentration comparison

```
# -*- coding: utf-8 -*-
"""
Created on Wed Apr 3 12:37:14 2019

@author: Khang Tran
"""

from __future__ import division
from __future__ import print_function

import pandas as pd
import numpy as np
import time
import cantera as ct

print("Running Cantera version: {}".format(ct.__version__))

#matplotlib notebook
import matplotlib.pyplot as plt




mechanism = 'C:\\Users\\esl1\\Desktop\\Ignition Delay Study\\PythonIgnitionDelayCode\\OSULSPImech.cti'
gas = ct.Solution(mechanism)


# Reactor parameters
residenceTime = 0.07 # s
reactorVolume = 30.5*(1e-2)**3 # m3

# Instrument parameters

# This is the "conductance" of the pressure valve and will determine its efficiency in
# holding the reactor pressure to the desired conditions.
pressureValveCoefficient = 0.01

# This parameter will allow you to decide if the valve's conductance is acceptable. If there
# is a pressure rise in the reactor beyond this tolerance, you will get a warning
maxPressureRiseAllowed = 0.01
# Simulation termination criterion
maxSimulationTime = 50 # seconds



# Define all the temperatures at which we will run simulations. These should overlap
# with the values reported in the paper as much as possible
T = [900,925,950,975,1000,1025,1050,1075,1100,1125,1150,1175,1200,1225,1250]




reactorPressure = 1.0*ct.one_atm # in atm. This equals 1.06 bars
inletConcentrations = {'C16H34': 0.0003, 'O2': 0.0147, 'N2': 0.985}
concentrations = inletConcentrations
```

```
fuelAirMixtureTank = ct.Reservoir(gas)
exhaust = ct.Reservoir(gas)

stirredReactor = ct.IdealGasReactor(gas, energy='off', volume=reactorVolume)

massFlowController = ct.MassFlowController(upstream=fuelAirMixtureTank,
                                    downstream=stirredReactor,
                                    mdot=stirredReactor.mass/residenceTime)

pressureRegulator = ct.Valve(upstream=stirredReactor,
                         downstream=exhaust,
                         K=pressureValveCoefficient)

reactorNetwork = ct.ReactorNet([stirredReactor])

# Now compile a list of all variables for which we will store data
columnNames = [stirredReactor.component_name(item) for item in range(stirredReactor.n_vars)]
columnNames = ['pressure'] + columnNames

# Use the above list to create a DataFrame
timeHistory = pd.DataFrame(columns=columnNames)
# Create a DataFrame to store values for the above points
tempDependence = pd.DataFrame(columns=timeHistory.columns)
tempDependence.index.name = 'Temperature'

for temperature in T:
    # Re-initialize the gas
    reactorTemperature = temperature # Kelvin
    reactorPressure = 1.0*ct.one_atm # in atm. This equals 1.06 bars
    reactorVolume = 30.5*(1e-2)**3 # m3

    gas.TPX = reactorTemperature, reactorPressure, inletConcentrations

    # Re-initialize the dataframe used to hold values
    timeHistory = pd.DataFrame(columns=columnNames)

    # Re-initialize all the reactors, reservoirs, etc.
    fuelAirMixtureTank = ct.Reservoir(gas)
    exhaust = ct.Reservoir(gas)

    # We will use concentrations from the previous iteration to speed up convergence
    gas.TPX = reactorTemperature, reactorPressure, concentrations

    stirredReactor = ct.IdealGasReactor(gas, energy='off', volume=reactorVolume)
    massFlowController = ct.MassFlowController(upstream=fuelAirMixtureTank,
                                        downstream=stirredReactor,
                                        mdot=stirredReactor.mass/residenceTime)
    pressureRegulator = ct.Valve(upstream=stirredReactor,
                             downstream=exhaust,
                             K=pressureValveCoefficient)
    reactorNetwork = ct.ReactorNet([stirredReactor])

    # Re-run the isothermal simulations
    tic = time.time()
    t = 0
    while t < maxSimulationTime:
        t = reactorNetwork.step()

    state = np.hstack([stirredReactor.thermo.P,
                       stirredReactor.mass,
                       stirredReactor.volume,
                       stirredReactor.T,
```

```
                    stirredReactor.thermo.X])

    toc = time.time()
    print('Simulation at T={}K took {:3.2f}s to compute'.format(temperature, toc-tic))

    concentrations = stirredReactor.thermo.X

    # Store the result in the dataframe that indexes by temperature
    tempDependence.loc[temperature] = state


export_csv = tempDependence.to_csv (r'C:\\Users\\esl1\\Desktop\\Ignition Delay Study\\PythonIgnitionDelayCode\\JSRcalcdata1atm0.5
      phi.csv', index = None, header=True)


expData = pd.read_csv('C:\\Users\\esl1\\Desktop\\Ignition Delay Study\\PythonIgnitionDelayCode\\JSRdata1atm0.5phi.csv')
expData.head()









plt.figure()
plt.plot(tempDependence.index, tempDependence['CO'], 'b>-', label='CO')
plt.plot(tempDependence.index, tempDependence['H2'], 'm^-', label='H$_{2}$')
plt.plot(tempDependence.index, tempDependence['O2'], 'r<-', label='O$_{2}$')
plt.plot(tempDependence.index, tempDependence['CO2'], 'y*-', label='CO$_{2}$')
plt.plot(tempDependence.index, tempDependence['C2H4'], 'g+-', label='C$_{2}$H$_{4}$')
plt.xlabel('Temperature (K)')
plt.ylabel(r'Mole Fractions')

plt.plot(expData['T/K'], expData['CO'],'b>', label='CO (exp)')
plt.plot(expData['T/K'], expData['H2'],'m^', label='H$_{2}$ (exp)')
plt.plot(expData['T/K'], expData['O2'],'r<', label='O$_{2}$ (exp)')
plt.plot(expData['T/K'], expData['CO2'],'y*', label='CO$_{2}$ (exp)')
plt.plot(expData['T/K'], expData['C2H4'],'g+', label='C$_{2}$H$_{4}$ (exp)')

plt.xlim([900, 1250])
plt.legend(loc='upper center', bbox_to_anchor=(1.2, 1));
```